UNIVERSIDADE FEDERAL FLUMINENSE

INSTITUTO DE QUÍMICA

PROGRAMA DE PÓS-GRADUAÇÃO EM GEOCIÊNCIAS - GEOQUÍMICA

KAROL DE OLIVEIRA DUARTE

DEGLACIAL TO HOLOCENE ANTARCTIC INTERMEDIATE WATER (AAIW) VARIABILITY IN THE SOUTHWESTERN ATLANTIC

NITERÓI

2020

KAROL DE OLIVEIRA DUARTE

DEGLACIAL TO HOLOCENE ANTARCTIC INTERMEDIATE WATER (AAIW) VARIABILITY IN THE SOUTHWESTERN ATLANTIC

Dissertação apresentada ao Curso de Pós-Graduação em Geociências da Universidade Federal Fluminense, como requisito parcial para a obtenção do Grau de Mestre. Área de Concentração: Geoquímica Ambiental.

Orientadora:

Profª Drª Ana Luiza Spadano Albuquerque

Coorientadora:

Drª Bruna Borba Dias

NITERÓI

2020

Ficha catalográfica automática - SDC/BGQ
Gerada com informações fornecidas pelo autor

D812d Duarte, Karol de Oliveira
Deglacial to Holocene Antarctic Intermediate Water (AAIW) variability in the Southwestern Atlantic / Karol de Oliveira Duarte ; Ana Luiza Spadano Albuquerque, orientadora ; Bruna Borba Dias, coorientadora. Niterói, 2020.
67 f. : il.

Dissertação (mestrado)-Universidade Federal Fluminense, Niterói, 2020.

DOI: http://dx.doi.org/10.22409/PPG-Geo.2020.m.13927535702

1. Paleoceanografia. 2. Foraminifero. 3. Oceano Atlantico Sul. 4. Produção intelectual. I. Albuquerque, Ana Luiza Spadano, orientadora. II. Dias, Bruna Borba, coorientadora. III. Universidade Federal Fluminense. Instituto de Química. IV. Título.

CDD -

Bibliotecária responsável: Catia Vasconcellos Marques - CRB7/5116

KAROL DE OLIVEIRA DUARTE

DEGLACIAL TO HOLOCENE ANTARTIC INTERMEDIATE WATER (AAIW) VARIABILITY IN THE SOUTHWESTERN ATLANTIC

Dissertação apresentada ao Curso de Pós - Graduação em Geociências da Universidade Federal Fluminense, como requisito parcial para a obtenção do **Grau de Mestre**. Área de Concentração: **Geoquímica Ambiental**.

Aprovada em março de 2020.

BANCA EXAMINADORA

PROF.ª DR.ª. ANA LUÍZA SPADANO ALBUQUERQUE
ORIENTADORA / UFF

DR.ª BRUNA BORBA DIAS
CO-ORIENTADORA / UFF

PROF.ª DR.ª. RUT AMELIA DÍAZ RAMOS
UFF

DR. DOUGLAS VILLELA LESSA
UFF

DR. IGOR MARTINS VENANCIO PADILHA DE OLIVEIRA
INPE

NITERÓI
2020

DEDICATION

I would like to dedicate this dissertation to my grandmother, Leonídia dos Santo Viveiros, who was a central figure in my education, always supporting me and my studies.

ACKNKOWLEGDEMENTS

Firstly, I would like to thank my advisors Ana Luiza Spadano Albuquerque and Bruna Borba Dias for giving me the opportunity to work in this project and for all the support during the two years of the program. Thank you very much for believing in me.

I am very grateful to all the colleagues and professors from the Geochemistry Graduate Program - UFF, for all the helpful advices and interesting discussions. My sincere thanks to all LOOP members, I will always carry the cheerful moments, research debates and amazing teamwork experiences with me. Additionally, I would like to give a special thanks to Diego Friande, for the all support during laboratory activities and analyzes, and to Carolina Santos, for all the times we discussed about our research topics together and helped each other.

My thanks to my family - my mother, father, grandmother, aunts, uncles and cousins - for all the emotional support through these two years of research. In particular, I would like to thank my mother for all the times she encouraged my curiosity and my will to learn, since my childhood.

Finally, I am grateful for CAPES and CNPq for providing the financing for this research project.

ABSTRACT

The Atlantic Intermediate Water (AAIW) plays an important role in the Atlantic Meridional Overturning Circulation (AMOC), as one of the water masses that contribute to the formation of North Atlantic Deep Water (NADW) in the high latitudes of the North Atlantic, and also because its northward flow counter-acts the southward flow of NADW and is an important part of the heat and salt transport between ocean basins. There are several studies that investigate the variations of AAIW and its influence in the AMOC over time, but very few focuses on the Holocene despite the increasing evidence for intermediate circulation changes in the mid-Holocene. In this study, we aimed to evaluate the dynamics of intermediate circulation in the Southwestern Atlantic through $\delta^{13}C$ and granulometry analyses. We have analyzed AAIW variations in intensity through the deglacial and Holocene using two cores (M125-78-2 - 845m depth, and M125-77-2 - 1394m depth) from the northeastern Brazilian coast. We have made radiocarbon-based age-models, sortable silt analyzes, $\delta^{13}C$ measurements from benthic (*Cibicidoides wuellestorfi*) and planktonic (*Neogloboquadrina dutertrei*) foraminifera and the $\delta^{13}C$ gradient ($\Delta\delta^{13}C_{pl\text{-}epi}$). Core M125-78-2 shows a strong shift in most variables approximately at 8ka BP, while core M125-77-2 has a more stable pattern, but also has a small shift in the $\delta^{13}C_{epi}$ and $\Delta\delta^{13}C_{pl\text{-}epi}$ starting at 8Ka BP. Comparison with data from other cores from the southeastern Atlantic reveals that the 8ka BP change coincides in timing with εNd evidence for an intensification of the AAIW circulation, and planktonic foraminifera geochemistry evidence for a southward shift of the westerlies. According to our data and the comparisons with previous studies, the southward movement of the westerlies increased the entrance of AAIW from the Pacific through the Drake Passage, intensifying the intermediate circulation of the southwestern Atlantic during the Holocene.

Keywords: Foraminifera. Paleoceanography. Antarctic Intermediate Water.

RESUMO

A Água Intermediária Antártica (AAIW) tem um papel fundamental na Célula de Revolvimento Meridional do Atlântico (do inglês *Atlantic Meridional Overturning Circulation*, AMOC), como uma das massas d'água que contribuem para a formação da Água profunda do Atlântico Norte (NADW) nas altas latitudes do Atlântico Norte, também porque o seu fluxo à norte contrabalanceia o fluxo à sul da NADW e é uma parte importante no transporte de calor e sal entre as bacias oceânicas. Há vários estudos que investigam as variações da AAIW e sua influência na AMOC ao longo do tempo, mas poucos focam no Holoceno apesar das crescentes evidências para mudanças na circulação intermediária durante o Holoceno médio. Nesse trabalho, nós visamos avaliar a dinâmica da circulação intermediária no Atlântico Sudoeste através de análises granulométricas e de $\delta^{13}C$. Analisamos as variações na intensidade da AAIW ao longo do deglacial e Holoceno usando dois testemunhos sedimentares da costa do nordeste do Brasil (M125-78-2 - 845m de profundidade e M125-77-2 - 1394m de profundidade). Fizemos modelos de idade com base em radiocarbono, análises de s*ortable silt,* $\delta^{13}C$ de foraminíferos planctônicos (*Neogloboquadrina dutertrei*) e bentônicos (*Cibicidoides wuellestorfi*) e o gradiente $\delta^{13}C$ ($\Delta\delta^{13}C_{pl\text{-}epi}$). O testemunho M125-78-2 mostra uma grande mudança na maioria das variáveis em aproximadamente 8 mil anos AP, enquanto o testemunho M125-77-2 tem um padrão mais estável, mas também com uma pequena variação no $\delta^{13}C_{epi}$ e $\Delta\delta^{13}C_{pl\text{-}epi}$ a partir de 8 mil anos AP. Comparações com dados de outros testemunhos do Atlântico sudeste revelaram que a mudança em 8 mil anos AP coincide em tempo com evidências de εNd para a intensificação da circulação da AAIW, e evidência de geoquímica de foraminíferos planctônicos para uma posição mais a sul dos ventos *westerlies*. De acordo com nossos dados e as comparações com estudos prévios, o movimento à sul dos *westerlies* aumentaram a entrada da AAIW proveniente do Pacífico pela Passagem de Drake, intensificando a circulação intermediária do Atlântico Sudoeste durante o Holoceno.

Palavras-chave: Foraminíferos. Paleoceanografia. Água intermediária Antártica

ABBREVIATIONS LIST

%HUM	Percentage of humidity of the sample
%SED	Percentage of sediment of the sample
AAIW	Antarctic Intermediate Water
ACC	Antarctic Circumpolar Current
AL	Agulhas Leakage
AMOC	Atlantic Meridional Overturning Circulation
AMS	Accelerator mass spectrometry
BC	Brazil Current
BFAR	Benthic Foraminifera Accumulation Rate
BMC	Brazil Malvinas Current
BP	Before present
CDW	Circumpolar Deep Water
D_d	Density of diluted sample
D-O	Dansgaard-Oeschger
DP	Drake Passage
D_r	Real density of the sample
et al.	et alii; and others
GNAIW	Glacial North Atlantic Intermediate Water

IPCC	Intergovernmental Panel on Climate Change
IRD	Ice-rafted debris
IRMS	Isotopic ratio mass spectrometer
IWBC	Intermediate Western Boundary Current
Ka	Kilo annum; thousand years
LGM	Last Glacial Maximum
NADW	North Atlantic Deep Water
NBC	North Brazil Current
SAC	South Atlantic Current
SACW	South Atlantic Central Water
SE	Southeastern
SEC	South Equatorial Current
S_i	Size fraction
SS	Sortable silte mean size
SW	Southwestern
TOC	Total Organic Carbon
TW	Tropical Water
UC Davis	University of California (Davis)
UK	United Kingdom
USA	United States of America
V_d	Volume of the sediment decantated

V_{rs}	Total volume of diluted sample (Bengal Rose solution + sediment)
W_d	Weight of dried solution
W_i	Weight in grams of each size fraction
W_r	Estimated real weight of dried sample
W_{rs}	Total weight of diluted sample (Bengal Rose solution + sediment)
W_t	Weight estimated for the non-diluted sample
$\delta^{13}C_{epi}$	$\delta^{13}C$ of epibenthic foraminifera tests
$\delta^{13}C_{pl}$	$\delta^{13}C$ of planktonic foraminifera tests
$\delta^{18}O_{epi}$	$\delta^{18}O$ of epibenthic foraminifera tests
$\Delta\delta^{13}C_{pl\text{-}epi}$	$\delta^{13}C$ gradient between planktonic and epibenthic foraminifera tests $\delta^{13}C$

ILLUSTRATIONS LIST

Figure 1 - Schematic representation of the global ocean circulation 19

Figure 2 - Living planktonic foraminifera.....23

Figure 3 - Foraminifera species used for geochemical analyses in this study 24

Figure 4 - Schematic representation of the superficial and intermediate circulation in the South Atlantic, and the location of the studied and mentioned cores 32

Figure 5 - Location map of the cores from this study.....33

Figure 6 - Section showing cores position in relation to the water masses vertical structure of the South Atlantic 34

Figure 7 - Age-models for core M125-78-2 and M125-77-2 39

Figure 8 - Sedimentation rates for cores M125-78-2 and M125-77-2.....41

Figure 9 - Stable Isotopes, Organic Matter, BFAR and Sortable Silt analyses results for cores M125-78-2 and M125-77-2.....43

Figure 10 - Benthic foraminifera $\delta^{13}C$ comparison.....45

Figure 11 - Data comparison between both cores of this study and other AAIW-bathed cores 48

Figure 12 - Records of $\delta^{13}C$ (planktonic and benthic foraminifera) and $\Delta\delta^{13}C$ across the deglaciation 51

TABLE LIST

Table 1 - Radiocarbon ages obtained from planktonic foraminifera analysis 38

Table 2 - Sedimentation rates and density of the sediment for core M125-78-2 39

Table 3 - Sedimentation rates and density of the sediment for core M125-77-2 40

SUMMARY

1 INTRODUCTION 13

2 OBJECTIVES 17

3 THEORETICAL BASIS 18

3.1 Ocean circulation 18

3.2 Foraminifera 22

3.3 Sortable Silt Proxy 28

4 STUDY AREA AND REGIONAL SETTINGS 30

5 METHODOLOGY 33

5.1 Depth-age models 35

5.2 Micropaleontological and Stable Isotopes Analyses 35

5.3 Benthic Foraminifera Accumulation Rate (BFAR) 36

5.4 Sortable Silte 37

5.5 Bulk organic matter geochemistry 37

6 RESULTS 38

7 DISCUSSION 44

7.1 Benthic foraminifera $\delta^{13}C$ viability as AAIW $\delta^{13}C_{DIC}$ proxy 44

7.2 $\Delta\delta^{13}C$ as evidence for a wind-driven AAIW intensity increase 50

8 CONCLUSIONS 54

9 REFERENCES 55

10 APPENDIX A – Tables of data from core M125-78-2 62

11 APPENDIX B – Tables of data from core M125-77-2 63

12 APPENDIX C – Sedimentological data Graphs 65

13 APPENDIX D – Rose Bengal diluted samples volume correction tables 66

14 APPENDIX E – BFAR graph with estimated benthic foraminifera individuals per cm^3 67

1 INTRODUCTION

Climate science has become of great importance in recent years, since global warming and the anthropogenic contribution to climate change was recognized as an impending problem. The IPCC Assessment Report (2014) classify as very probable an increase in species extinction, ocean acidification, and global mean sea level rise, to name a few problems related to global warming. In order to develop better models to predict the future climate, it is necessary to improve the understanding of the present climate mechanisms. However, it is not enough to perform measurements of present climate conditions, since instrumental measurements of climatic parameters such as temperature and salinity only reach back to about 350 years (IPCC, 2013). Because of this, it is necessary to find ways to recover longer time series to comprehend climatic changes beyond that recorded by human instruments. Providing information regarding how climate evolved due to orbital changes, continental drift, glaciation, and other processes involved in climate variability and its triggers is essential, and these data may be used to estimate future climate change, its effects on society and possible mitigation actions.

The functioning of Earth's climate involves several complex relations amongst atmosphere, hydrosphere, biosphere, lithosphere and cryosphere. In this regard, the ocean circulation plays a key role to maintain the energetic equilibrium of the planet, transporting heat and salt among the ocean basins and between the tropics and the poles (RAHMSTORF, 2002). In this context, the Atlantic circulation is of great importance for the global climate, transporting heat and salt from the South Atlantic northwards, until the higher latitudes of the Northern Hemisphere. The Atlantic Ocean circulation is the only oceanic cell in which the net flux of heat and salt flows completely northwards, instead of the expected Equator-to-poles flux (GORDON, 1986; RINTOUL, 1991). In this ocean basin occurs a circulation cell that comprises both North and South Atlantic, the Atlantic Meridional Overturning Circulation (AMOC), which transports warm, superficial waters northwards and cold, deep waters southwards (GORDON, 1986; RINTOUL, 1991; RAHMSTORF, 2002; RAHMSTORF, 2006; RHEIN, 2019).

One of the water masses involved in this circulation cell is the Antarctic Intermediate Water (AAIW), a low-salinity and low temperature intermediate-depth water mass that is formed by subduction of cold and low-salinity waters near the

Antarctic Polar Front, in the southeastern Pacific and southwestern Atlantic (TALLEY, 1996; TALLEY, 1999; GARABATO et al., 2009; VOIGT et al., 2016). AAIW plays an important role in the AMOC, as one of the water masses that contribute to the formation of North Atlantic Deep Water (NADW) in the high latitudes of the North Atlantic, also because its northward flow counter-acts the southward flow of NADW and is an important part of the heat transport between ocean basins (TALLEY, 1999; GARABATO et al., 2009).

Several works highlight the importance of understanding AAIW variations, but there are not many studies that track AAIW variations over several glacial-interglacial cycles (PAHNKE; ZAHN, 2005; RONGE et al., 2015). In the Southwestern Pacific, off the coast of New Zealand, Pahnke and Zahn (2005) have found a decrease in benthic $\delta^{13}C$ during glacial periods, which they related to the strengthening of the southern westerlies, that increased the northward transport of freshwater and, consequently, the buoyancy at the Subantarctic Zone, reducing the AAIW formation. A more recent study, however, hypothesized that the northward advancement of the sea-ice edge and, consequently, the northward displacement of the southern westerly winds induced a reduction in the AAIW formation in the SW Pacific under glacial conditions, thus resulting in a shallowing of AAIW during glacial times (RONGE et al., 2015, and references therein).

Most studies focus on the Last Glacial Maximum (LGM) and the deglaciation, especially during the North Atlantic cold events, the Heinrich Stadial 1 - 14.5 to17.5 ka BP - and Younger Dryas - 11.7 to 12.9 ka BP (RICKABY; ELDERFIELD, 2005; HENDRY et al., 2012; HUANG et al., 2014; LIPPOLD et al., 2016; HOWE et al., 2016; OPPO et al., 2018; UMLING et al., 2019), however, only a few of them address the Holocene variability (LIPPOLD et al., 2016; HOWE et al., 2016; VOIGT et al., 2016). Most studies focus on the dynamics between NADW production and the AAIW formation and spreading towards the North Atlantic, about which several authors propose a ‘see-saw’ model for the Atlantic circulation, wherein reduced formation of deep waters in the North Atlantic during cold-climate periods would intensify the formation of AAIW in the Southern Ocean, and the contrary during warm-climate periods (BROECKER, 1998; PAHNKE et al., 2008; ANDERSON et al., 2009; BLUNIER; BROOK, 2011).

The see-saw model was recently contested by Howe et al. (2016), that finds no evidence in Neodymium isotopes of cores from the Southwestern Atlantic of increased intensity of the AAIW during the deglaciation. Instead, there is evidence of an increased AAIW intensity during the mid-Holocene (HOWE et al., 2016; LIPPOLD et al., 2016). Voigt et al. (2016) have also found evidence in sortable silt, which is used to trace the intensity of bottom water currents, that AAIW intensity raised at approximately 7ka BP. The possible mechanisms for this mid-Holocene intensification are still in debate, since Howe et al. (2016) proposed a wind-driven mechanism, in which the westerlies would have increased AAIW formation or increased Pacific waters influence, while Voigt et al. (2016) defend that a cooling in the Southern Ocean lead to increased convection and formation rates.

Also, changes in the paleoproductivity are expected to have being reflected in the AAIW, since AAIW carries nutrients from the Southern Ocean northwards (SIGMAN et al., 2010). Studying paleoproductivity changes during the millennial-scale cold events, Hertzberg et al. (2016) observed that the variation of $\delta^{13}C$ gradient was compatible with an overall reduction in the biological pump efficiency due to the weakening of the AMOC. This gradient can be used to evaluate the efficiency of the biological pump, in a way that increased vertical transport of organic matter should increase the $\delta^{13}C$ gradient, and vice versa. Although not the focus of their work, the reconstruction from Hertzberg et al. (2016) shows an interesting feature in the southwestern Atlantic: the $\delta^{13}C$ gradient shows an evident decrease in the mid-Holocene (~8 ka BP) that is not present in any other ocean basin. Interestingly, the timing of this variation is compatible with evidence for an intensification of AAIW during the Holocene (HOWE et al., 2016; VOIGT et al., 2016).

Summarizing, AAIW variability, even though still poorly understood, has a great potential to influence the AMOC intensity, the Atlantic primary productivity and, consequently, the ocean-atmosphere CO_2 exchange. Therefore, it is of great importance to improve our knowledge about AAIW past changes and triggers, in order to improve circulation models and future climate estimations. This study focuses on the deglacial to Holocene variability of AAIW dynamics, and what mechanisms could be driving it. We hypothesized that AAIW variability is driving the changes in the $\delta^{13}C$ gradient of the southwestern Atlantic during the Holocene. We also present geochemical and sedimentological evidence for AAIW intensification in the mid-

Holocene and discuss the possible mechanisms that could drive such circulation change and its effects on the $\delta^{13}C$ gradient.

2 OBJECTIVES

This project aims to evaluate the variability of intermediate water circulation in the Southwestern Atlantic during the deglacial and Holocene, along with possible driving mechanisms. To achieve this result, we will:

- Prepare depth-age models for two cores using radiocarbon analyses in planktonic foraminifera tests;
- Reconstruct the $\delta^{13}C_{DIC}$ of intermediate and superficial water by performing stable isotopes analyses in foraminifera tests;
- Reconstruct the vertical carbon transportation in the water column using the $\Delta\delta^{13}C_{pl\text{-}epi}$, the $\delta^{13}C$ gradient;
- Estimate de intensity of bottom currents at intermediate depths using the sortable silt proxy;
- Integrate the circulation and carbon transport proxies, comparing with pre-existing data, to analyze the dynamics and variability of Southwestern Atlantic intermediate circulation.

3 THEORETICAL BASIS

3.1 Ocean circulation

Surface ocean circulation is mainly driven by wind forcing, that together with the Coriolis effect – a force that happens due to the Earth's rotation and deflects the water masses' movements to the right in the Northern Hemisphere and to the left in the Southern Hemisphere – form subtropical gyres in the oceanic basins (RAHMSTORF, 2002; RUDDIMAN, 2014). Deep-ocean circulation, however, depends on thermal and salinity-related mechanisms, called the thermohaline circulation. A part of the warm surface water escapes the subtropical gyres, flowing towards the poles and carrying heat (RAHMSTORF, 2002; RAHMSTORF, 2006; RUDDIMAN, 2014). At the high latitudes, these surface waters lose heat to the overlying cold atmosphere, becoming colder and denser (RAHMSTORF, 2002; RUDDIMAN, 2014). Additionally, the formation of sea ice increases the salinity and density of the water due to salt rejection (RUDDIMAN, 2014). The denser water sinks, filling the deeper portions of the oceanic basins. The combination of wind-driven and density-driven processes result in the ocean circulation cells (Figure 1).

Figure 1 - Schematic representation of the global ocean circulation

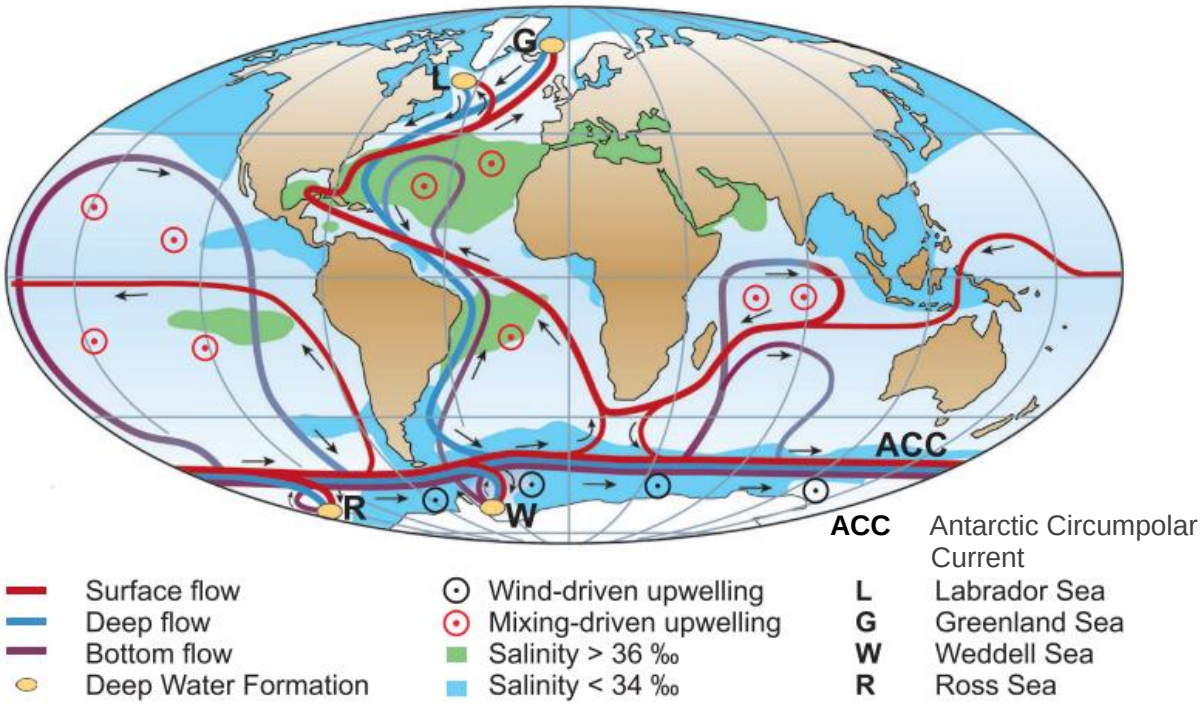

SOURCE: RAHMSTORF, 2006.

The AMOC is one of the most important circulation cells that makes the distribution of heat and salt. This cell transports the warm water from the tropics to the high latitudes of the Northern Hemisphere through the superficial waters of the Gulf Stream (RHEIN, 2019). In two regions of the North Atlantic, at the Labrador Sea and the north of Iceland, these superficial waters lose heat to the cold air masses from the Arctic, while the formation of sea ice increases the salinity. As the water becomes colder and saltier, the density increases until it sinks, forming the NADW, which flows south, towards the Antarctic, at depths between approximately 1200 and 3500m (GORDON, 1986; RAHMSTORF, 2006). When NADW reaches the Southern Ocean, it upwells, entering the Antarctic Circumpolar Current and joining the eastward flow around Antarctica.

To counteract the southward flow of the NADW and the water output from the Atlantic, there is a contrary superficial flow northward, towards the North Atlantic. Water enters the South Atlantic through two possible ways: the Agulhas leakage, south of Africa, and the Drake Passage, south of South America. The northward flow in the Atlantic is performed by the intermediate flow of the AAIW (TALLEY, 1999; GARABATO et al., 2009). This water mass is formed in the subpolar region, in the

Southwestern Atlantic, flowing northwards with the Malvinas (Falklands) Current, until the Brazil-Malvinas Confluence, where a major part of it turns eastwards and enters the Subtropical Gyre (RINTOUL, 1991). When it reaches the tropics, a part of the AAIW flows into the North Atlantic, where it feeds the superficial waters, that will eventually reach the high latitudes, closing the circulation cell.

This is the present-day functioning, but the ocean circulation was subjected to alterations due to several mechanisms over time, acting on different timescales. Tectonic forcings happen over the longer time scales (10^6 – 10^9 years) and alter ocean circulation by changing the continents position, opening and closing oceanic pathways. The glacial-interglacial oscillations occurs over time-scales of 10^4 to 10^5 years and are triggered by Earth's orbital movements (eccentricity, obliquity and precession), which affect the total amount and seasonal distribution of solar radiation received in the surface, changing the energy imbalance between the poles and the tropics (BERGER et al., 2005; SPIEGEL et al, 2010; RUDDIMAN, 2014).

Superimposed on the longer timescales oscillations it can also be identified more abrupt oscillations, on a millennial-scale (10^3 years), of the climate system during the glacial periods: the Dansgaard-Oeschger Oscillations (or D-O events), characterized by a rapid increase in temperature, until almost interglacial conditions, followed by a progressive return to glacial temperatures (BROECKER, 1994; MCMANUS et al., 1999; RUDDIMAN, 2014). Associated to D-O events are also recognized events of freshwater discharge into the North Atlantic, related to the colder periods of the D-O oscillations, probably a result of the destabilization of glaciers, that have enlarged during the cold periods and caused the depression of underlying bedrock until allowing the sea water to enter underneath the glacier margin, leading to ice melting and liberation of icebergs (MACAYEAL, 1993; BROECKER, 1994). These events are named Heinrich Events, which are characterized by an abrupt increase in the ice-rafted debris (IRD), identified in marine sediment cores (HEINRICH, 1988; BROECKER, 1994; RUDDIMAN, 2014).

Regarding the cold events, they are mainly recognized in the North Atlantic, but they find opposite equivalents in the Southern Ocean: the cold events of *Heinrich Stadial* 1 (~16,5 ka) and *Younger Dryas* (~12 ka) coincide with the deglacial warming of Antarctica, while the warm period in the North Hemisphere, called Bølling-Allerød,

coincides with a cold period in the South Hemisphere, the Antarctic Cold Reversal (BROECKER, 1994; ANDERSON et al., 2009; BLUNIER; BROOK, 2011).

Several studies have shown that the AMOC has varied its intensity over time (MCMANUS et al., 2004; BÖHM et al., 2015). Böhm et al. (2015) support that during glacial periods the AMOC was weaker/shallower, because a decrease in density of the North Atlantic surface waters would cause less sinking and thus less NADW formation, restricting this water mass to intermediate depths of ~2km, known as *Glacial North Atlantic Intermediate Water*, or GNAIW. Several studies (BROECKER, 1998; SAENKO et al., 2003; PAHNKE et al., 2008; ANDERSON et al., 2009; BLUNIER; BROOK, 2011) propose that, similarly to the temperature, AMOC also would work the opposite way in the North and South Hemispheres, the see-saw model: an increase/decrease in the formation of NADW is related to the decrease/increase in the AAIW formation. Therefore, glacial conditions would have increased AAIW formation and its propagations towards the North Atlantic (PAHNKE et al., 2008; LIPPOLD et al., 2016). This see-saw model was recently contested, however, by some studies that did not find evidence of the AAIW expansion in the Southwestern Atlantic during the deglaciation (HOWE et al., 2016; LIPPOLD et al., 2019).

AMOC oscillations through time are prone to cause alterations in other circulation-related mechanisms, such as the productivity, in the Atlantic. The Southern Ocean surface waters receive nutrients from the upward flowing deeper water masses, but the organisms do not use up all these nutrients, due to limiting conditions, especially iron and solar radiation (SIGMAN et al., 2010). These unused nutrients in the surface waters can be downwelled during the formation of AAIW, thus the variability of AAIW nutrient content has the potential to alter the ocean-atmosphere CO_2 equilibrium through the biological pump efficiency of the Southern Ocean, a key region for the CO_2 exchange (SIGMAN et al., 2010; HERTZBERG et al., 2016).

The biological pump is the mechanism through which the CO_2 concentrations between the oceans and the atmosphere are coupled: biological productivity in the surface uses the CO_2 dissolved in the water to produce organic matter, and the sinking of this material transports carbon towards deeper waters, where it can be deposited in the sediments or remineralized into dissolved CO_2, and the removal of CO_2 from the surface ocean results in more atmospheric CO_2 being dissolved into the ocean, reducing the CO_2 pressure of the atmosphere (SHARP, 2007; SIGMAN; HAUG, 2003).

The biological pump efficiency depends on the amount of available nutrients in the water, principally nitrogen and phosphorous, the main limiting nutrients to the aquatic organisms (SIGMAN; HAUG, 2003).

The coupling between ocean circulation and the CO_2 pressure in the atmosphere means it is of great importance to better understand how AMOC varies over time, in particular with relation to intermediate circulation, to provide better constrains to climatic models.

In order to obtain the necessary data on modern and paleocirculation, it is usually necessary to make use of proxies to acquire indirect measurements on several parameters, such as temperature, salinity, carbon transport, etc. Analyzing carbonate shells secreted by marine organisms, such as foraminifera, is a common way to obtain chemical and biological data that can be used for calculating several proxies (KATZ et al., 2010).

3.2 Foraminifera

Foraminifera are single-celled eukaryotes, ameboid-like protozoans, usually marine organisms, but some forms can also be found in brackish waters (Goldstein, 1999; SCHIEBEL; HEMLEBEN, 2017; BOUDAGHER-FADEL, 2015). These organisms have an elaborate solid outer shell, also called test, normally made of secreted carbonate ($CaCO_3$, calcite or aragonite), but some species form their tests from secreted silica, organic substances, or agglutinated sediment particles, and sizes vary from less than 100µm to several centimeters (SCHIEBEL; HEMLEBEN, 2017; BOUDAGHER-FADEL, 2015). Foraminifera tests are frequently perforated, divided in chambers, the number of chambers increase as the organism grows, and most of the cytoplasm lives inside the test (BOUDAGHER-FADEL, 2015). A part of the cytoplasm is also extended outside the shell through the pores as pseudopodia, which are used for nourishment (GOLDSTEIN, 1999; BOUDAGHER-FADEL, 2015). Symbiont-barren species feed on planktonic organisms or organic particles, while symbiont-bearing species receive energy partly via photosynthesis and partly via predation (BOLTOVSKOY; WRIGHT, 2013; BOUDAGHER-FADEL, 2015) (Figure 2).

Figure 2 - Living planktonic foraminifera

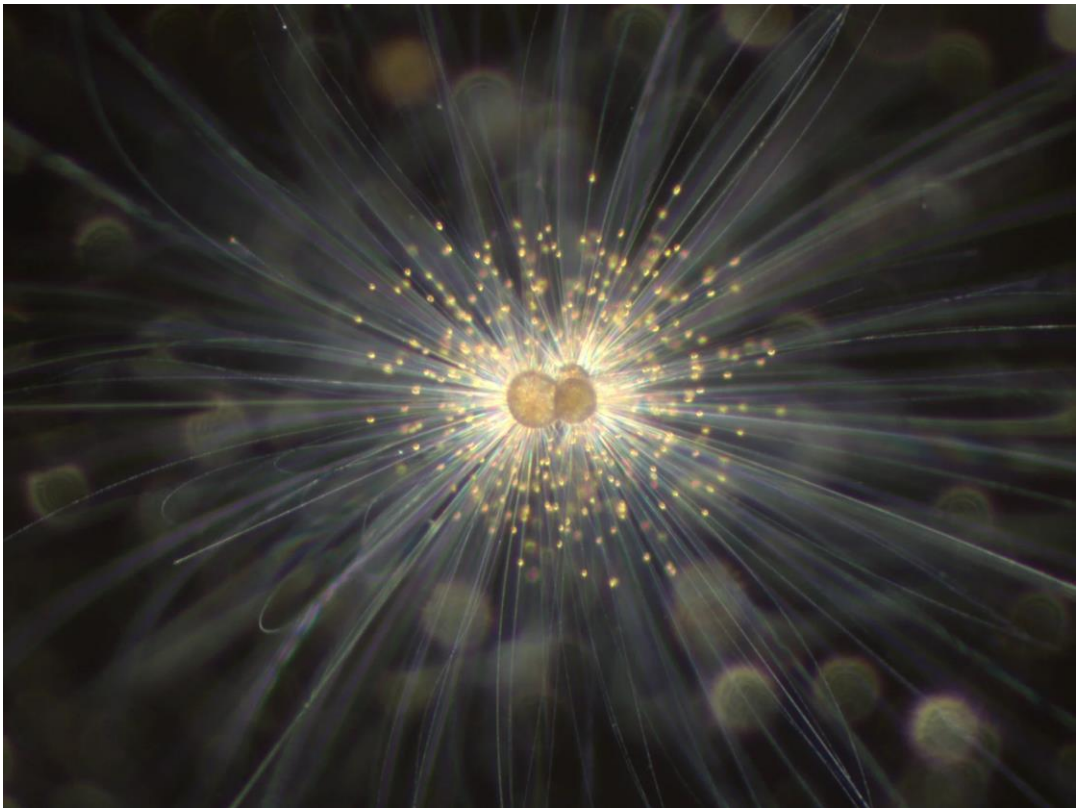

CAPTION: The long filaments are pseudopodia, and the golden dots are symbionts.
SOURCE: https://factsfromthefield.wordpress.com/2015/10/28/what-are-foraminifera/

Foraminifers are divided according to two different living strategies: benthic foraminifera and planktonic foraminifera. Benthic foraminifera firstly appeared in the Cambrian Period, and inhabit a variety of environments, from brackish and shallow waters to deep-sea (BOUDAGHER-FADEL, 2015). They can live attached to the substrate surface, the epifaunal species, or inside the sediment, the infaunal species, and usually feed on organic particles that sink from the surface. The planktonic foraminifera evolved in the Jurassic Period, and are an important part of the marine plankton, feeding on plankton or photosynthesis via symbionts (BOUDAGHER-FADEL, 2015; SCHIEBEL; HEMLEBEN, 2017).

Due to the variety of environments where they can be found, large range in the geological time, and the high preservation rate of their calcareous tests, the foraminifers have a great potential for being used in reconstructions in paleoceanography, paleoecology, and paleoclimate studies (BOLTOVSKOY; WRIGHT, 2013; BOUDAGHER-FADEL, 2015; SCHIEBEL; HEMLEBEN, 2017) (Figure 3). As such, foraminifera can be used as proxies - in other words, as an indirect

way to quantify/estimate a variable that cannot be directly measured - for several physical, chemical, and environmental variables (MURRAY, 2001; BOUDAGHER-FADEL, 2015).

Figure 3 - Foraminifera species used for geochemical analyses in this study

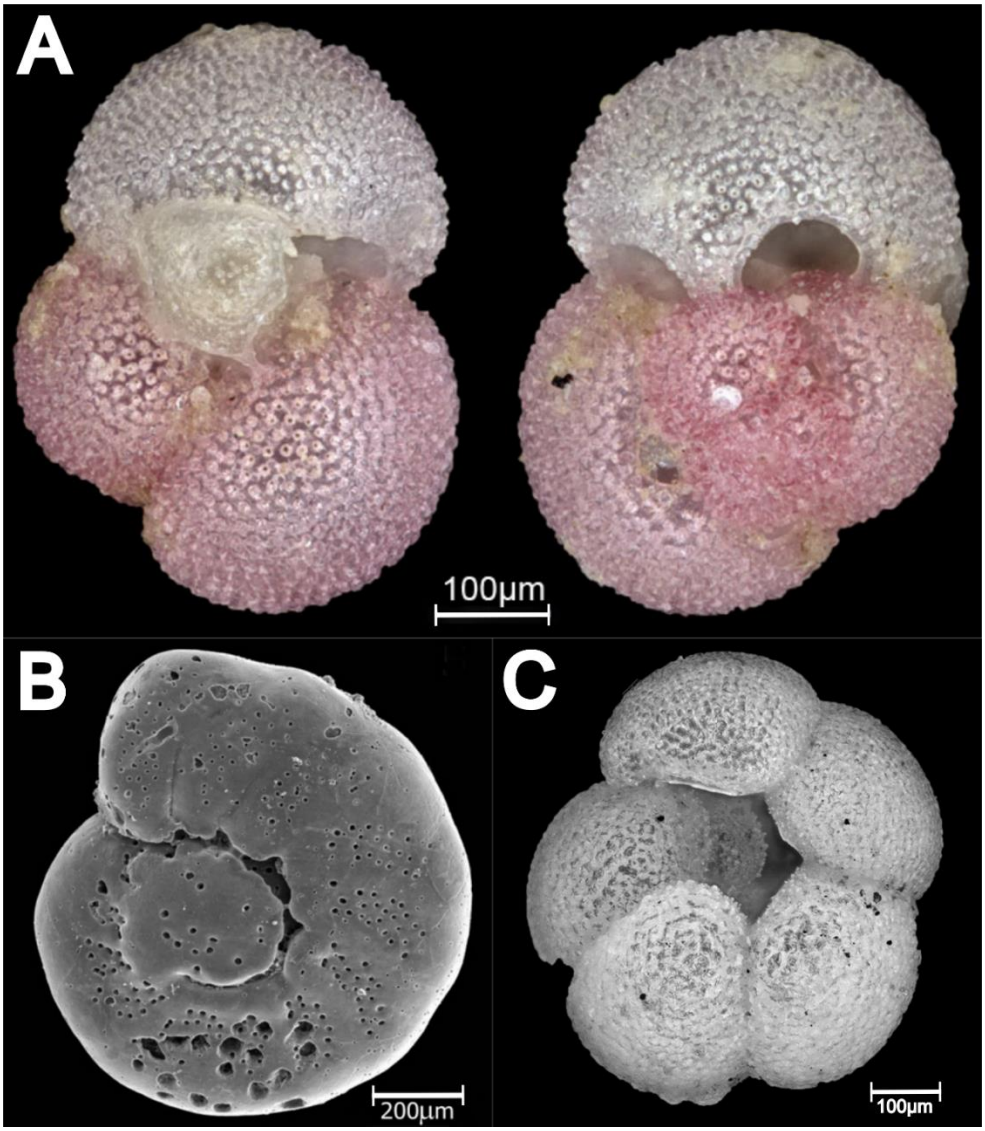

CAPTION: (A) Planktonic foraminifera *Globigerinoides ruber*, (B) Benthic foraminifera *Cibicidoides incrassatus*, (C) Planktonic foraminifera *Neogloboquadrina dutertrei*.
SOURCE: foraminifera.eu

Foraminifera can be used as proxies in two ways: the chemistry of their shells, in which the composition of the tests is analyzed and the proportion of certain elements (such as magnesium and cadmium) can be used as an estimate of an environmental parameter (water temperature and nutrient content, respectively), and the biological

way, because foraminifera assemblages respond to environmental changes, such as temperature, salinity, food supply, and others (MURRAY, 2001; KATZ et al.,2010).

In this study, we made use of two proxies, chemical analyses of the $\delta^{13}C$ of planktonic and benthic foraminifera tests, along with a faunal proxy of benthic foraminifera, the Benthic Foraminifera Accumulation Rate (BFAR), as a productivity estimation.

Stable isotopes on foraminifera tests are useful as several proxies, including sea water temperature, salinity, and productivity (SHARP, 2007; KATZ et al.,2010). Isotopes measured in the $CaCO_3$ of the shells are ^{18}O, ^{16}O, ^{13}C and ^{12}C. The lighter isotopes are naturally more abundant, but the amount of the heavier isotopes (^{18}O and ^{13}C) in relation to the lighter isotopes (^{16}O and ^{12}C) in the foraminifera shell depends on several factors, including temperature, salinity, dissolved inorganic carbon (DIC) content in the water, and vital effects as a result of the metabolism (SHARP, 2007; KATZ et al.,2010). The process of altering the relative quantities of light and heavy isotopes due to some environmental/ biological parameter is called fractionation and is the base for stable isotopes analyses (SHARP, 2007). By measuring the ratio between light and heavy isotopes, it is possible to estimate variations in the parameter that may affect the ratio.

Stable isotopes analyses are made in terms of isotope ratios and the comparison of isotopic compositions between the sample and a reference standard, because relative differences can be measured with greater precision than absolute atom counts (SHARP, 2007). The stable isotopes ratio difference is reported in the delta (δ) notation, which is:

$$\delta^{13}C = \left(\frac{{}^{13}C/{}^{12}C_{sample} - {}^{13}C/{}^{12}C_{standard}}{{}^{13}C/{}^{12}C_{standard}} \right) \times 1000$$

$$\delta^{18}O = \left(\frac{{}^{18}O/{}^{16}O_{sample} - {}^{18}O/{}^{16}O_{standard}}{{}^{18}O/{}^{16}O_{standard}} \right) \times 1000$$

The δ notation is expressed in per mil (‰), as a convenient way to represent differences that are usually small (SHARP, 2007).

The $\delta^{13}C$ values of the planktonic foraminifera tests reflect the $\delta^{13}C_{DIC}$ of the surface ocean water, but also can be affected by vital effects, symbionts' photosynthesis and surface productivity (KATZ et al., 2010). Due to all these processes that could affect the $\delta^{13}C$ signal, the analyzed species must be chosen carefully. Symbiont-barren planktonic foraminifera such as *Neogloboquadrina dutertrei*, that lives in the high nutrient and high productive zones, can closely reflect the $\delta^{13}C_{DIC}$ of the water (HILBRETCH, 1997, and references therein). However, symbiont-bearing species, like *Globigerinoides ruber*, usually found in clear water and oligotrophic conditions, can show $\delta^{13}C$ deviations from the water when switching between predation and photosynthesis-derived energy, as photosynthesis uptakes the ^{12}C and leaves the microambient enriched in ^{13}C, causing the shell to have a higher $\delta^{13}C$ values than that of the DIC (SCHIEBEL; HEMLEBEN, 2017).

The $\delta^{13}C$ values of the epifaunal benthic foraminifera reflect the $\delta^{13}C_{DIC}$ of the near bottom-water, which is a result of the mixing between the $\delta^{13}C_{DIC}$ of the water mass and the remineralization of the organic matter sinking from the upper ocean (KATZ et al., 2010). As mentioned previously, the primary productivity in the surface ocean uses preferentially light carbon, when the carbon fixated through photosynthesis is exported to deeper waters it is remineralized, releasing light carbon and lowering the $\delta^{13}C_{DIC}$ values of the intermediate and deep-ocean (MACKENSEN, 2004), which is recorded by the benthic foraminifera tests. But benthic foraminifera $\delta^{13}C$ can also be affected by other processes, such as phytodetrital deposition and vital effects.

Phytodetrital deposition occur in high productivity events and could affect the $\delta^{13}C$ of benthic foraminifera tests as a result of the respiration of ^{13}C-depleted organic matter on the surface of the sediment. Seasonal high productivity could release light carbon, impoverishing in ^{13}C the sediment-water interface, and be recorded in the $\delta^{13}C$ of epibenthic foraminifera, such as *Cibicidoides* and related genera, yielding a more depleted value then that from the actual water mass $\delta^{13}C_{DIC}$ (MACKENSEN et al., 1993; ZARRIESS; MACKENSEN, 2011). So, caution must be taken when using the $\delta^{13}C$ value of benthic foraminifera and a proxy in high productivity zones.

The $\delta^{13}C_{DIC}$ can yield several information, such as tracking water masses and mixing rates. Intermediate and deep waters are isolated from direct exchange with atmospheric CO_2, so the $\delta^{13}C_{DIC}$ can only be altered by mixing different water masses or the “aging” effect, in which the $\delta^{13}C_{DIC}$ becomes more depleted in ^{13}C because of organic matter oxidation in the water column, though the $\delta^{13}C$ alone is not enough due to all factors that can alter its value and is used together with other proxies (CURRY; OPPO, 2005). Remineralization can also be estimated using $\delta^{13}C_{DIC}$ reconstructions by comparison between the $\delta^{13}C$ of epifaunal and infaunal benthic foraminifera. Infaunal benthic foraminifera incorporate the carbon of the pore water, which is dependent on the sinking of organic matter and the remineralization in the sediment, consequently the higher the $\delta^{13}C$ of infaunal foraminifera, the more remineralization on the sediment and the lower the food supply (KATZ et al., 2010).

A proxy often used for approximating ocean paleoproductivity variations is the $\delta^{13}C$ gradient between surface and deep water, or $\Delta\delta^{13}C$ (KATZ et al., 2010). Surface ocean phytoplankton fixates the dissolved carbon into organic compounds during photosynthesis. The primary production uses up preferentially the light carbon isotope ^{12}C, because metabolic reactions require less energy to break ^{12}C bonds than heavier isotope ^{13}C bonds (SHARP, 2007). Consequently, as the phytoplankton grows, the ^{12}C is incorporated and removed from the dissolved carbon pool of the surface ocean, resulting in an increased $\delta^{13}C_{DIC}$ (MACKENSEN, 2004; KATZ et al., 2010).

When planktonic organisms die, their organic matter slowly sinks toward the bottom waters, and while a major part of the organic matter is remineralized in the water column, a small fraction reaches the surface of the sediment and serves as food supply for benthic organisms, such as benthic foraminifera (BURDIGE, 2007; KATZ et al., 2010). The remineralization of organic matter releases the light carbon, depleting the ^{13}C the DIC of the bottom water mass (MACKENSEN, 2004; KATZ et al., 2010). Thus, the more primary production at the surface ocean, the higher will become the surface $\delta^{13}C_{DIC}$, while the lower the bottom water $\delta^{13}C_{DIC}$ will be. As such, the gradient (difference) between the $\delta^{13}C$ from planktonic and benthic foraminifera raises when the surface ocean productivity increases, and vice-versa.

Another way to investigate paleoproductivity is by analyzing the foraminifera assemblages. The Benthic Foraminifera Accumulation Rate (BFAR) is a biological

proxy that relates the number of benthic foraminifera in the sediment sample to the surface ocean paleoproductivity (HERGUERA; BERGER, 1991).

Since the bottom ocean environment is less susceptible to temperature and salinity variations, the benthic foraminifera assemblages are responsive especially to two factors: oxygen and food supply (MURRAY, 2001). Both factors are related to the organic particle flux from the surface ocean, since the benthic organisms feed on the organic matter particles and the respiration of organic matter consumes oxygen (MURRAY, 2001; KATZ et al., 2010).

Of course, it is not enough to simply count the benthic foraminifera in each sediment sample, because the sedimentation rates vary along the core, and the density of the sediment usually increases with depth, consequently the same volume of two samples, one at the bottom of the core and one at the core top, amount for different time ranges. Thus, the estimation of number of benthic foraminifera per gram of sediment (ind.g) is taken in proportion to the sedimentation rate ($cm.ka^{-1}$) and sediment density ($g.cm^{-3}$) of each sample. Therefore, the BFAR index yields a number $ind.cm^{-2}.ka^{-1}$.

3.3 Sortable Silt Proxy

The deposition and sorting of the sediments is highly dependent of the strength and viscosity of the current in which they are being transported (MCCAVE et al., 1995; MCCAVE, 2008). Thus, stronger currents can transport coarser sediment, and as the current loses its velocity, the coarser sediments are deposited first. As most of the bottom ocean sediment is constituted by silt and clay-sized particles, the difference in the deposition of these size fractions could be used as a current strength indicator.

The silt fraction comprehends the sediment with sizes between 63 and 10 µm, but this size fraction shows to different behaviors to bottom current dynamics. The silt fraction coarser than 10µm, the sortable silt fraction, behaves more similarly to sand (>63 µm), that is, in a non-cohesive manner, while the fraction finer than 10µm behaves like clay (<2 µm) (MCCAVE et al., 1995; MCCAVE, 2008). Clay particles have a cohesive behavior so that, once settled, it requires a much stronger current to detach then from one another, and thus the clay does not respond proportionately to the

bottom current hydrodynamics (MCCAVE et al., 1995; MCCAVE, 2008). Larger particles, such as sortable silt and sand particles, on the contrary, are less susceptible to form aggregates (MCCAVE, 2008). Therefore, the amount and proportion of the sortable silt fraction responds to the dynamics of the bottom current and can be used as proxy for paleocurrent intensity variations. (MCCAVE et al., 1995; MCCAVE, 2008).

4 STUDY AREA AND REGIONAL SETTINGS

This study is based on two cores collected from the northeastern Brazilian slope, offshore the Rio de Contas mouth (Figures 4 and 5). In this region, the shelf is narrower and shallower than in other parts of the Brazilian continental margin, with an average width of 30km and average depth of 40m (MARTINS; COUTINHO, 1981). The slope is also relatively abrupt, with 30km of average width (MARTINS; COUTINHO, 1981).

Geostrophic circulation in the South Atlantic is mainly influenced by the Subtropical Gyre, which transport water masses eastwards through the South Atlantic Current (SAC), and then westwards via the South Equatorial Current (SEC) (STRAMA; ENGLAND, 1999; BOEBEL et al., 1999) (Figure 4). When reaching the Brazilian margin, a part of the water flows southwards along the Brazil Current (BC), which is one of the South Atlantic western boundary currents, representing the principal superficial current that flows southwards along the Brazilian coast, between ~8-10° and ~40°S. Another part turns Equatorward, entering the North Brazil Current (NBC) flowing toward the Equatorial Atlantic (STRAMA; ENGLAND, 1999). When the BC encounters the Malvinas (Falklands) Current at ~40°S, its flow turns eastwards, moving away from the coast and entering the SAC (STRAMA; ENGLAND, 1999; SILVEIRA et al., 2000; VOIGT et al., 2015). The first studies about the intermediate water flow did not include AAIW as a part of the Subtropical Gyre and considered that it flowed northward along the coast. However, several subsequent works concluded that AAIW flows northward until the Brazil-Malvinas Confluence, and then a major fraction flows eastward following the anticyclonic gyre (RINTOU, 1991; SILVEIRA et al., 2000; GARABATO et al., 2009) (Figure 4).

Superficial oceanic flow in the study area is mostly influenced by the BC, transporting the Tropical Water (TW), above 250m, and the South Atlantic Central Water (SACW), between 300 and 500m depth, both high salinity and temperature water masses (TW: >20°C, >36.0 psu; SACW: 20-6°C, 36.0-34.6 psu) (VIANA et al., 1998; SILVEIRA et al., 2000) (Figure 6). TW and SACW flow along the Subtropical Gyre, bifurcating when they reach the Brazilian margin at ~15°S and ~20°S, respectively (STRAMA; ENGLAND, 1999) (Figure 4).

The AAIW and Circumpolar Deep Water (CDW) flow between 550m and 1200m water depth, both low temperature and salinity water masses (3-6°C, 34.6-34.2 psu) that come from the Southern Ocean and are rich in nutrients and dissolved oxygen, when compared to the superficial water and the NADW (VIANA et al., 1998; SILVEIRA et al., 2000) (Figure 6). Also, there is a part of AAIW formed in the Pacific Ocean does not enters the Pacific circulation, flowing south from its formation region (SE Pacific), and entering the Atlantic through the Drake Passage (Figure 4) (GORDON, 1986; LAMY et al., 2015). For this study we referred both AAIW and CDW water masses as AAIW, because it was not possible to differentiate between both water masses with our data. The geostrophic flow from intermediate waters is different from that of superficial waters masses in a way that, at this depth, the Subtropical Gyre is latitudinally narrower, and the AAIW bifurcates at ~25°S (STRAMA; ENGLAND, 1999) (Figure 4). Most of the AAIW then flows southwards with the BC, while above 25°S the flow is northwards, entering the Intermediate Western Boundary Current (IWBC) (STRAMA; ENGLAND, 1999; BOEBEL et al., 1999).

Underneath, between ~1200 and ~3500m depth, is the NADW, a high salinity and low temperature water mass from the North Atlantic, poor in nutrients (4-3°C, 34.6-35.0 psu) (VIANA et al., 1998; SILVEIRA et al., 2000) (Figure 6).

Figure 4 - Schematic representation of the superficial and intermediate circulation in the South Atlantic, and the location of the studied and mentioned cores

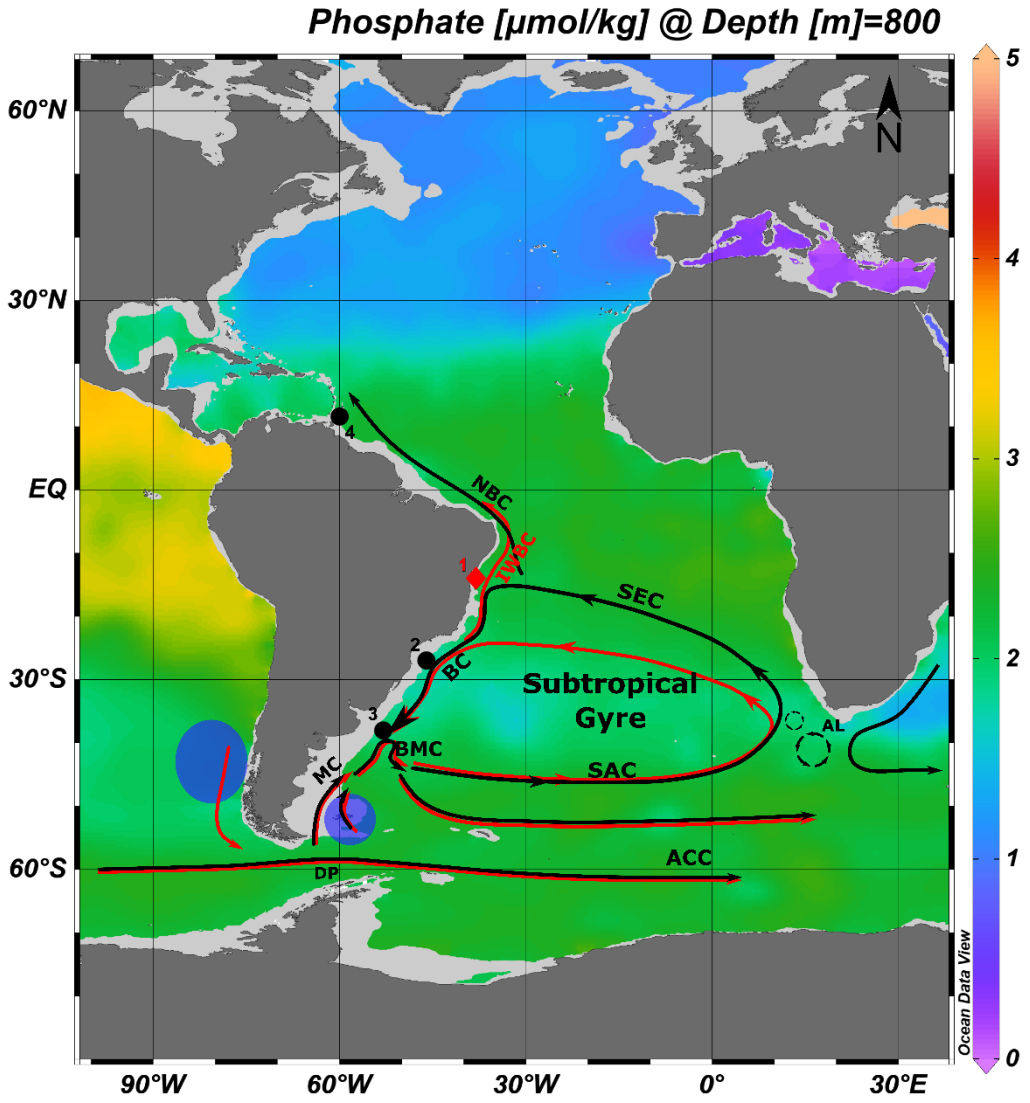

CAPTION: Map of the phosphate concentration (µmol/kg) at 800m depth, location of the studied cores and other records discussed in this paper and schematic representation of the superficial (black) and intermediate (red) circulation of the South Atlantic (STRAMA; ENGLAND, 1999; BOEBEL et al., 1999; GORDON, 1986; LAMY et al., 2015). 1: M125-77-2 and M125-78-2 (red diamond, this study); 2: cores KNR159-5-36GGC (27.5°S, 46.5°W, 1268m; UMLING et al., 2019), KNR159-5-90GGC (27.35°S, 46.63°W, 1108m; CURRY; OPPO [2005] and UMLING et al. [2019]), KNR159-5-78GGC (27.5°S, 46.3°W, 1829m, HERTZBERG et al., 2016), GeoB2107-3 (27.17°S, 46.45°W, 1048m; PORTILHO-RAMOS et al., 2018, and HOWE et al., 2016), GeoB2104-3 (27.3°S, 46.4°W, 1500m, HOWE et al., 2016); 3: GeoB1386-1 (VOIGT et al., 2015); 4: M78/1-235-1 (POGGEMANN et al.,2017); Blue circles: approximate position of AAIW formation sites. DP – Drake Passage; AL – Agulhas leakage; ACC – Antarctic Circumpolar Current; SAC – South Atlantic Current; SEC – South Equatorial Current; IWBC – Intermediate Western Boundary Current; MC – Malvinas Current; BC – Brazil Current; NBC – North Brazilian Current; BMC – Brazil Malvinas Confluence. Phosphate at 800m depth marks the approximate extent of AAIW into the North Atlantic. Image was created using the database World Ocean Atlas (BOYER et al., 2013) and using the Ocean Data View software (SCHLITZER, R., Ocean Data View, odv.awi.de, 2020).
SOURCE: Prepared by the author, 2020.

5 METHODOLOGY

The collection of the two multicore-type oceanic sedimentary cores used in this study was performed during the M125 expedition of the German R/V Meteor. The cores M125-77-2 and M125-78-2 were collected at 14°23.200'S, 38°43.551'W and 14°24.356'S, 38°50.070'W, respectively (Figure 5). The former was collected at 1394.4m and the later at 845.2m water depth. Core M125-78-2 is located in the central portion of the AAIW, while core M125-77-2 is the transition zone between the AAIW and the underlying NADW (Figure 6). Both cores are 25cm long and were sliced every 1cm, except for the top, which was sliced in two parts of 0.5cm, yielding 26 samples per core. Bulk analyses were performed every centimeter for the top 10cm and every 2cm for the remaining samples. Granulometry, stable isotopes and benthic foraminifera assemblage analyses were executed for every sample in core M125-77-2, but were only analyzed for samples until 15cm depth in core M125-78-2.

Figure 5 - Location map of the cores from this study

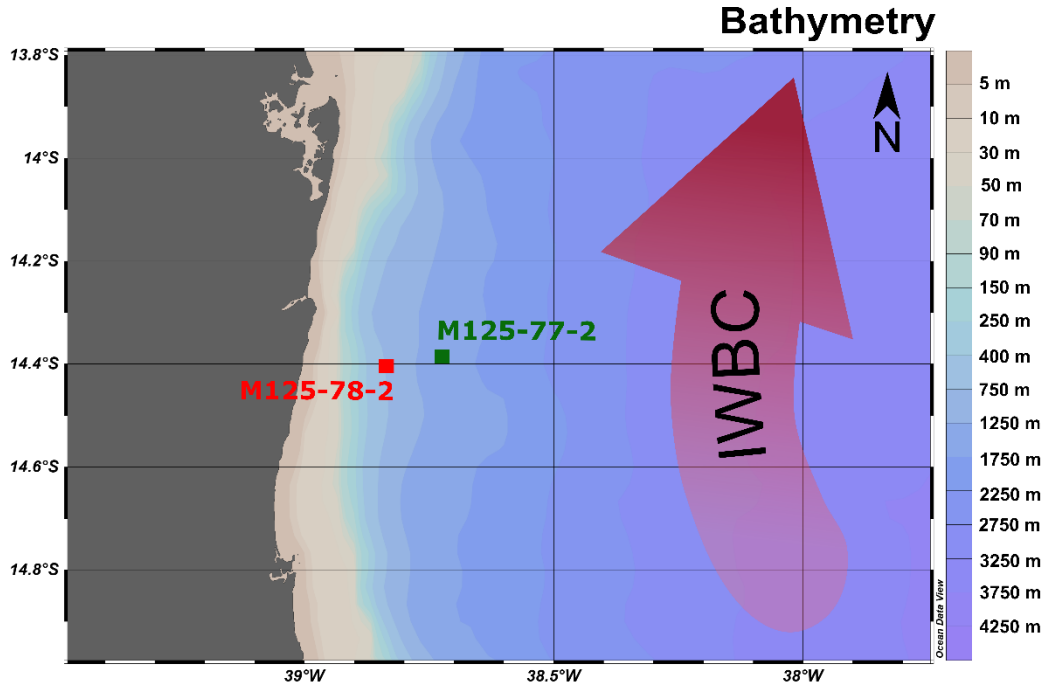

CAPTION: Cores location off the Brazilian northeastern margin: M125-78-2, 845.2m depth (red) and core M125-77-2, 1394.4m depth (green). The image also shows the intermediate current flow direction. Image was created using the Ocean Data View software (SCHLITZER, R., Ocean Data View, odv.awi.de, 2020).
SOURCE: Prepared by the author, 2020.

Figure 6 - Section showing cores position in relation to the water masses vertical structure of the South Atlantic

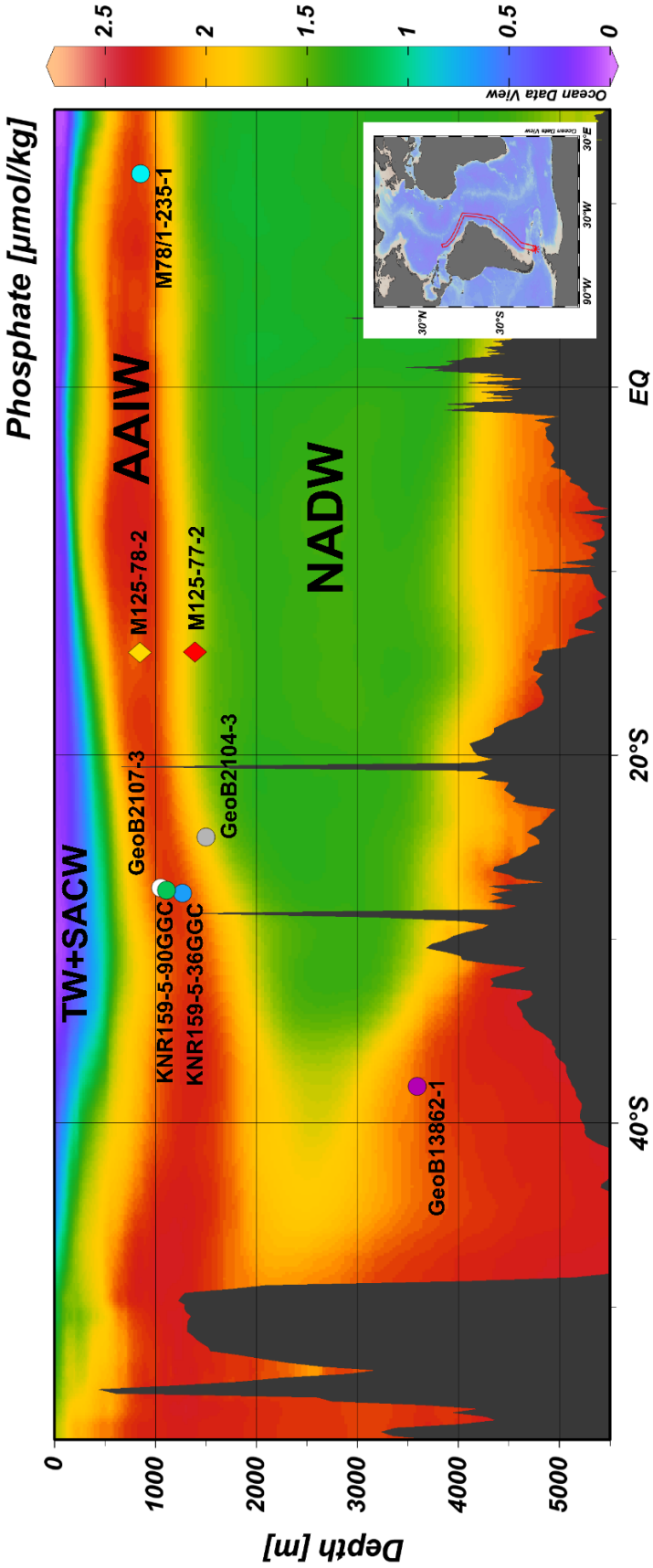

CAPTION: Section of modern phosphate concentration, showing the position of the cores from this study and those used for data comparison in relation to the water masses in the South Atlantic. *Yellow diamond*: core M125-78-2 (845.2); *red diamond*: core M125-77-2 (1394.4m); *light blue circle*: M78/1-235-1 (POGGEMANN et al.,2017; 850m); *blue circle*: cores KNR159-5-36GGC (UMLING et al., 2019; 1268m); *green circle*: KNR159-5-90GGC (UMLING et al., 2019; 1108m); *white circle*: GeoB2107-3 (HOWE et al., 2016 and PORTILHO-RAMOS et al., 2018; 1048m); *gray circle*: GeoB2107-3 (HOWE et al., 2016; 1500m); *purple circle*: GeoB1386-1 (VOIGT et al., 2015; 3588m). Image was created using the database World Ocean Atlas (BOYER et al., 2013) and using the Ocean Data View software (SCHLITZER, R.., Ocean Data View, odv.awi.de, 2020).
SOURCE: Prepared by the author, 2020

5.1 Depth-age models

The depth-age models for both cores were based on AMS (accelerator mass spectrometry) radiocarbon dating of planktonic foraminifera *Globigerinoides ruber* tests, 5 samples for core M125-77-2 and 7 samples for core M125-78-2. AMS dating was carried out at the Beta Analityc Laboratory (Florida, USA) (see Table 1). The specimens analyzed were bigger than 250µm, and the samples had approximately 8mg. The AMS ^{14}C ages were calibrated with the curve IntCal13 (Reimer et al., 2013), with a reservoir effect of 400 ± 200 (Balmer et al., 2016). The age models were generated with the Bacon package version 2.2 (Blaauw & Christen, 2011) for R software, with a setup based on Mulitza et al. (2017) [ssize=nmc*1.5, d.min=0, d.max=26, d.R=400, d.STD=200, mem.mean=0.7, mem.strength=4, acc.shape=1.5, acc.mean=500, res=10, t.a=9, t.b=10, depths.file=TRUE, prob=0.95]. (Figure 7).

5.2 Micropaleontological and Stable Isotopes Analyses

In order to perform the analyses, each 20cm³ sediment sample was wet-sieved with a 63µm sieve to separate the sediment and the foraminifera, and dried in a 50°C oven. Foraminifera were hand-picked using a small wet brush and a stereomicroscope, after fractionating the sediment into a manageable size. Identification was made based on Jones (1994).

Stable isotopes analyses ($\delta^{13}C$ and $\delta^{18}O$) were performed at UC Davis Stable Isotope Laboratory, with an Optima IRMS autocarb system in dual inlet mode, for two foraminifera species: planktonic foraminifera *Neogloboquadrina dutertrei* ($\delta^{13}C_{pl}$ and $\delta^{18}O_{pl}$), and benthic foraminifera *Cibicidoides incrassatus* (epifaunal - $\delta^{13}C_{epi}$ and $\delta^{18}O_{epi}$). Samples had between 2 and 7 specimens bigger than 250µm. All results are reported in parts per mil (‰) relative to the VPDB (Vienna Pee Dee Belemnite). Deviations for the stable isotope analyses were 0.04‰ for the $\delta^{13}C$ and 0.05‰ for $\delta^{18}O$.

We then calculated the $\delta^{13}C$ gradient ($\Delta\delta^{13}C_{pl\text{-}epi}$) for evaluating the paleoproductivity as a proxy for organic carbon exportation in the water column, using it for inferences regarding the biological pump efficiency (Hertzberg et al., 2016).

5.3 Benthic Foraminifera Accumulation Rate (BFAR)

The benthic foraminifera amount per sample was assessed fractionating the sediment until it was possible to count at least 300 specimens, and this counting was used to estimate the number of foraminifera in 1cm³ of sediment. The estimates were applied to calculate the Benthic Foraminifera Accumulation Rate (BFAR), which shows a high correlation with primary productivity and carbon exportation to the seafloor (HERGUERA; BERGER, 1991).

Because the first 11 samples for each core (0 to 10 cm) were diluted in a Bengal Rose solution (used for a different study) so it was necessary to correct the volume of the sediment (see Appendix D). We have firstly used a separated, non-diluted sample to calculate the real density (D_r) (Tables 2 and 3) and the percentage of sediment (%SED) and humidity (%HUM) for each sample. Then, we let a volume of the sediment and Rose Bengal solution to decant and measured the sediment volume (V_d). This volume was dried in a Becker with a known weight, so that we could calculate the weight of the dried solution (W_d). Wd and %SED were used to calculate the total weight expected if the sample wasn't diluted (W_t):

$$W_t = \frac{W_d \times 100}{\%SED}$$

W_t and V_d can be used for deriving the density of the diluted sediment (D_d):

$$D_d = \frac{W_t}{D_d}$$

The next step was to use the total volume (Bengal Rose + sediment) (V_{rs}) of the sample and multiply by D_d to obtain the weight of the diluted sample (W_{rs}):

$$W_{rs} = D_d \times V_{rs}$$

Finally, W_{rs} was converted into the real weight of the dried sample (W_r) by subtracting the percentage of humidity. W_r was multiplied by D_r to yield the real of the sediment sample (V_r):

$$W_r = W_{rs} - \left(\frac{W_{rs} \times \%HUM}{100}\right)$$

$$V_r = W_r \times D_r$$

The samples below 10cm were not diluted, so they did not need this correction and the number of benthic foraminifera was calculated using the tests obtained from the wet-sieving process (see section 4.2). The estimated individuals per cm^3 of all samples was transformed into individuals per gram by multiplying the density of the sediment, and this value was applied in the BFAR calculation:

$$Ind/_{cm^3} \times cm^3/_g = Ind/_g$$

BFAR ($ind.cm^{-2}.ka^{-1}$) was calculated as the estimated individuals of benthic foraminifera in 1g multiplied by the density and the sedimentation rates for each sample.

$$BFAR = Ind/_g \times g/_{cm^3} \times cm/_{ka}$$

5.4 Sortable Silte

The sortable silt (SS), mean grain size fraction between 10 and 63µm, was used as a proxy for evaluating the water mass intensity. Grain size was determined in a CILAS laser particle analyzer at the Geochemistry Department of Universidade Federal Fluminense, in decarbonated and oxided-organic matter samples. The sortable silt mean size fraction (µm) was calculated as:

$$SS = \frac{\sum_{10 \leq i \leq 63} S_i \times W_i}{\sum_{10 \leq i \leq 63} W_i}$$

In which S_i is the size fraction and W_i is the weight in grams of each fraction.

5.5 Bulk organic matter geochemistry

Total organic carbon (TOC) was also analyzed, in a PDZ Europa ANCA-GSL elemental analyzer interfaced to a PDZ Europa 20-20 isotope ratio mass spectrometer (IRMS) (Sercon Ltd., Cheshire, UK) at University of California (Davis). Measurements were performed in decarbonated and macerated sediment samples. Samples were combusted to 1000°C in a reactor with chromium oxide and silvered copper oxide, which were removed afterwards in a reduction reactor (reduced copper at 650°C). The helium carrier and the gases flow to the water trap, and after that the CO_2 is separated on a Carbosieve GC column (65°C, 65 mL/min).

6 RESULTS

The radiocarbon ages and calibrated ages used to produce the depth-age models for cores M125-78-2 and M125-77-2 are presented in Table 1 and Figure 7. Core M125-78-2 spans the period from 17.7ka to 2.18ka BP, while core M125-77-2 ages range between 22.7ka and 1.66ka BP. The age model for core M125-77-2 do not present any outlying dates. Core M125-78-2 shows two outlying ages, at 17 and 24 cm, which were not incorporated by the Bacon v2.2 to the final depth-age model due to Student-t model detection of outlier values (BLAAUW; CHRISTEN, 2011).

Table 1 - Radiocarbon ages obtained from planktonic foraminifera analysis

Core	Code	Depth (cm)	^{14}C Age (yrs BP)	Uncertainty (yrs)	Maximum age (cal yrs BP)	Minimum age (cal yrs BP)	Calibrated age (cal yrs BP)	Probability (%)
M125-77-2	Beta - 504071	0.5	1890	30	2045	1858	2330	95.4
M125-77-2	Beta - 504072	4	2820	30	3186	2970	3260	95.4
M125-77-2	Beta - 493665	10	8060	30	9239	9011	8500	95.4
M125-77-2	Beta - 504073	17	11580	40	13588	13335	12020	95.4
M125-77-2	Beta - 493666	24	19410	70	23662	23113	19850	95.4
M125-78-2	Beta - 504074	0.5	2470	30	2759	2603	2910	95.4
M125-78-2	Beta - 519332	5	5220	30	6171	5968	5660	95.4
M125-78-2	Beta - 493667	10	6010	30	7071	6850	6460	95.4
M125-78-2	Beta - 519333	15	6480	30	7493	7346	6910	95.4
M125-78-2	Beta - 504075	17	11810	40	13843	13536	12240	95.4
M125-78-2	Beta - 519334	20	13230	50	16120	15742	13660	95.4
M125-78-2	Beta - 493668	24	13260	40	16147	15786	13690	95.4

CAPTION: data in black were used in the age-depth modelling, while data in red were considered outlying values by the Bacon and were not incorporated.
SOURCE: Prepared by the author, 2020.

Figure 7 - Age-models for core M125-78-2 and M125-77-2

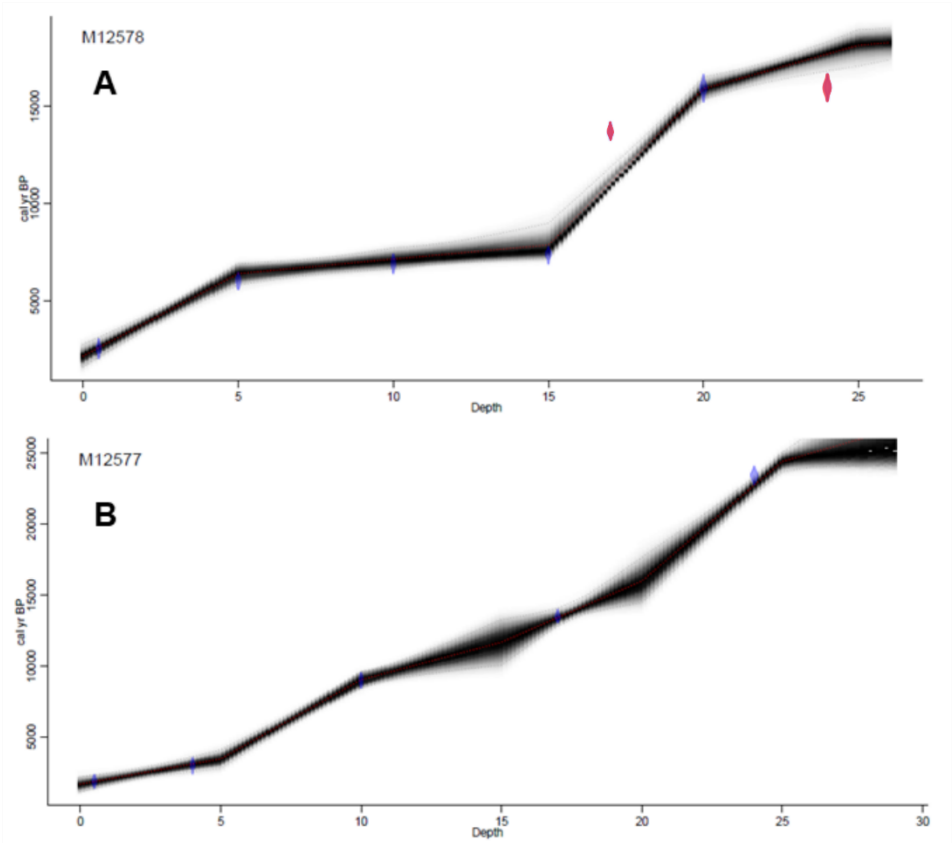

CAPTION: (A) Age model for core M125-78-2. (B) Age Model for core M125-77-2. Blue and red areas represent the probabilistic curves of the calibrated ages. Red curves were not considered in the model.
SOURCE: Prepared by the author, 2020.

Core M125-77-2 shows smaller sedimentation rates than core M125-78-2, ranging between 0.59 to at most 5.56cm/ka, with two periods of higher sedimentation: ~16 to -9.5ka and ~3.5 to 2ka (Table 3 and Figure 8). Core M125-78-2 reveals high sedimentation rates downcore, between ~8 to 6.5ka, and small rates towards the top, with a value range from 8.10 to 1.18cm/ka (Table 2 and Figure 8).

Table 2 - Sedimentation rates and density of the sediment for core M125-78-2

Core	Depth (cm)	Age yrs BP (median)	Sedimentation Rate (cm/ka)	Density (g/cm^3)
M125-78-2	0-0.5	2183.4	2.14	0.955
M125-78-2	0.5-1	2605.9	1.18	0.714
M125-78-2	1-2	3027.3	2.37	0.854
M125-78-2	2-3	3871.3	1.18	0.926
M125-78-2	3-4	4720.3	1.18	0.935
M125-78-2	4-5	5567.8	1.18	0.836

M125-78-2	5-6	6412.3	1.18	1.005
M125-78-2	6-7	6558.9	6.82	0.877
M125-78-2	7-8	6703.1	6.93	0.952
M125-78-2	8-9	6849.4	6.84	1.004
M125-78-2	9-10	6994.9	6.87	0.990
M125-78-2	10-11	7137.1	7.03	0.830
M125-78-2	11-12	7278.1	7.09	0.669
M125-78-2	12-13	7413.3	7.40	0.678
M125-78-2	13-14	7540.9	7.84	0.686
M125-78-2	14-15	7664.3	8.10	0.693

SOURCE: Prepared by the author, 2020.

Table 3 - Sedimentation rates and density of the sediment for core M125-77-2

Core	Depth (cm)	Age yrs BP (median)	Sedimentation Rate (cm/ka)	Density (g/cm^3)
M125-77-2	0-0.5	1667	1.77	0.401
M125-77-2	0.5-1	1846	2.79	0.718
M125-77-2	1-2	2026	5.56	0.787
M125-77-2	2-3	2383	2.80	0.600
M125-77-2	3-4	2736	2.83	0.545
M125-77-2	4-5	3088	2.84	0.565
M125-77-2	5-6	3438	2.86	0.576
M125-77-2	6-7	4557	0.89	0.725
M125-77-2	7-8	5677	0.89	0.784
M125-77-2	8-9	6790	0.90	0.738
M125-77-2	9-10	7905	0.90	0.859
M125-77-2	10-11	9019	0.90	0.761
M125-77-2	11-12	9553	1.87	0.663
M125-77-2	12-13	10086	1.88	0.703
M125-77-2	13-14	10616	1.89	0.744
M125-77-2	14-15	11137	1.92	0.753
M125-77-2	15-16	11658	1.92	0.762
M125-77-2	16-17	12518	1.16	0.770
M125-77-2	17-18	13380	1.16	0.779
M125-77-2	18-19	14232	1.17	0.741
M125-77-2	19-20	15079	1.18	0.704
M125-77-2	20-21	15925	1.18	0.689
M125-77-2	21-22	17622	0.59	0.689
M125-77-2	22-23	19318	0.59	0.675
M125-77-2	23-24	21016	0.59	0.722
M125-77-2	24-25	22711	0.59	0.769

SOURCE: Prepared by the author, 2020.

Figure 8 - Sedimentation rates for cores M125-78-2 and M125-77-2

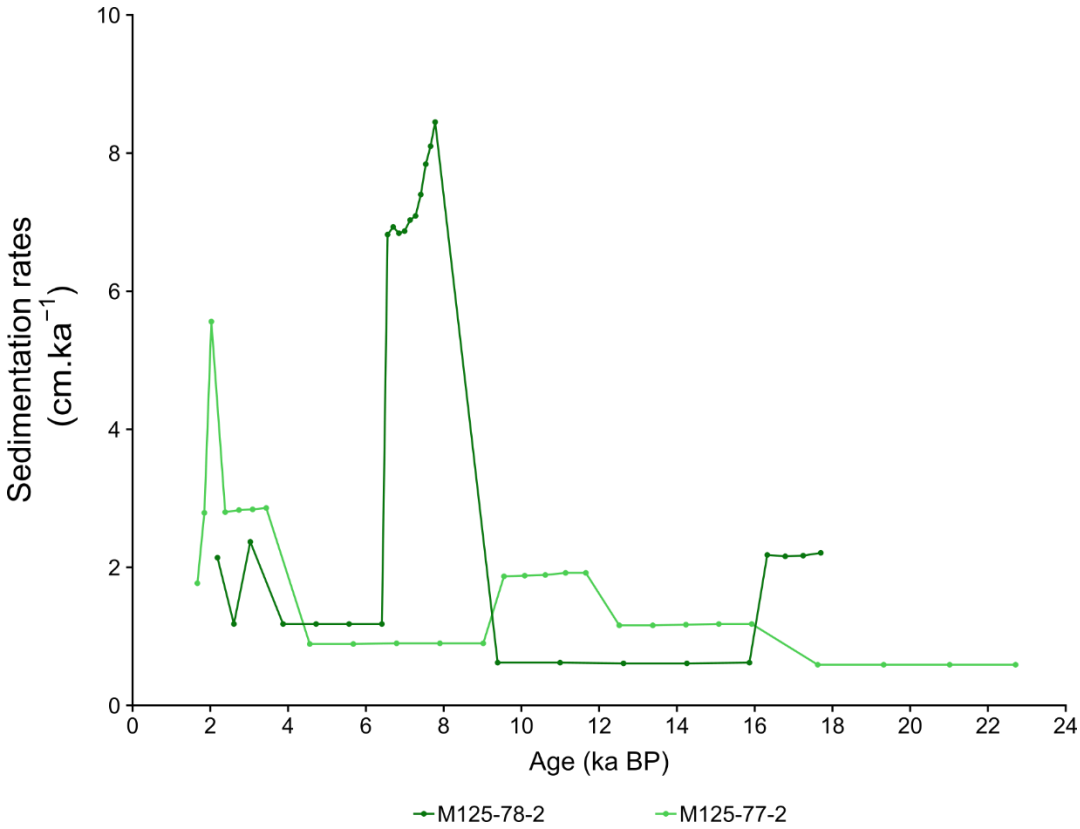

SOURCE: Prepared by the author, 2020.

Planktonic foraminifera carbon isotopes from core M125-77-2 shows values ranging from 1.31 to 2.24 ‰, with up to ~0.5‰ variations along the last deglaciation, while core M125-78-2 $\delta^{13}C_{pl}$ values range between 1.41 and 2.24‰. In the mid-Holocene, both cores reveal a depletion trend (Figure 9). *Cibicidoides incrassatus* carbon isotopes from core M125-77-2 range from 0.91 to 1.49‰ along the deglacial. Core M125-78-2 $\delta^{13}C_{epi}$ shows an increasing trend, with values ranging from 0.87 to 1.52‰, reaching its peak at approximately 5.5ka (Figure 9). Core M125-78-2 benthic foraminifera $\delta^{18}O$ range from 2.04 to 3.28‰ without a clear trend, while M125-77-2 $\delta^{18}O_{epi}$ decreases along the core, from ~4 to 2.14‰ (Figure 9).

The planktonic-benthic gradient for core M125-77-2 ranged from 0.33 to 1.25‰ in the deglacial. In core M125-78-2, $\Delta\delta^{13}C_{pl\text{-}epi}$ varies from 0.01 to1.37‰. Both cores show decreasing values $\Delta\delta^{13}C_{pl\text{-}epi}$ of the between 8 and ~6ka (Figure 9).

Core M125-77-2 TOC ranges between 0.55 and 1.86%, and shows two major TOC percentage peaks, the first at around 9ka BP (~1.43%) and the second in the late-Holocene (~1.5%), starting around 4ka BP. Core M125-78-2 TOC shows a

decrease in the mid-Holocene (~0.60%), followed by a late-Holocene increase (~1.15%) (Figure 9).

Core M125-78-2 sortable silt values reveal an abrupt increase around 7 ka, from ~16µm before the early Holocene up to 32µm in the mid- to late-Holocene. Sortable silt in core M125-77-2 shows a large variation, values ranging between 25.58 and 11.90µm during the deglacial, but an abrupt variation similar to that of core M125-78-2 is not present at this depth for the mid-Holocene (Figure 9).

BFAR values from core M125-78-2 shows variation from 10,813 up to 130,090 ind.cm^{-2}.ka^{-1}. A prominent feature of this core is the increase of the BFAR in the mid-Holocene, going from values around 50,000 ind.cm^{-2}.ka^{-1} around 8ka, up to ~130,000 ind.cm^{-2}.ka^{-1} at its peak around 7ka, between 6.5 and 3ka values decrease to ~15,000 ind.cm^{-2}.ka^{-1}, increasing again in the last two samples, at ~2.5ka (Figure 9 and Appendix E). Core M125-77-2 BFAR values vary between 778 and 12,811 ind.cm^{-2}.ka^{-1}, and only shows two peaks in the late-Holocene (Figure 9 and Appendix E).

Figure 9 - Stable Isotopes, Organic Matter, BFAR and Sortable Silt analyses results for cores M125-78-2 and M125-77-2

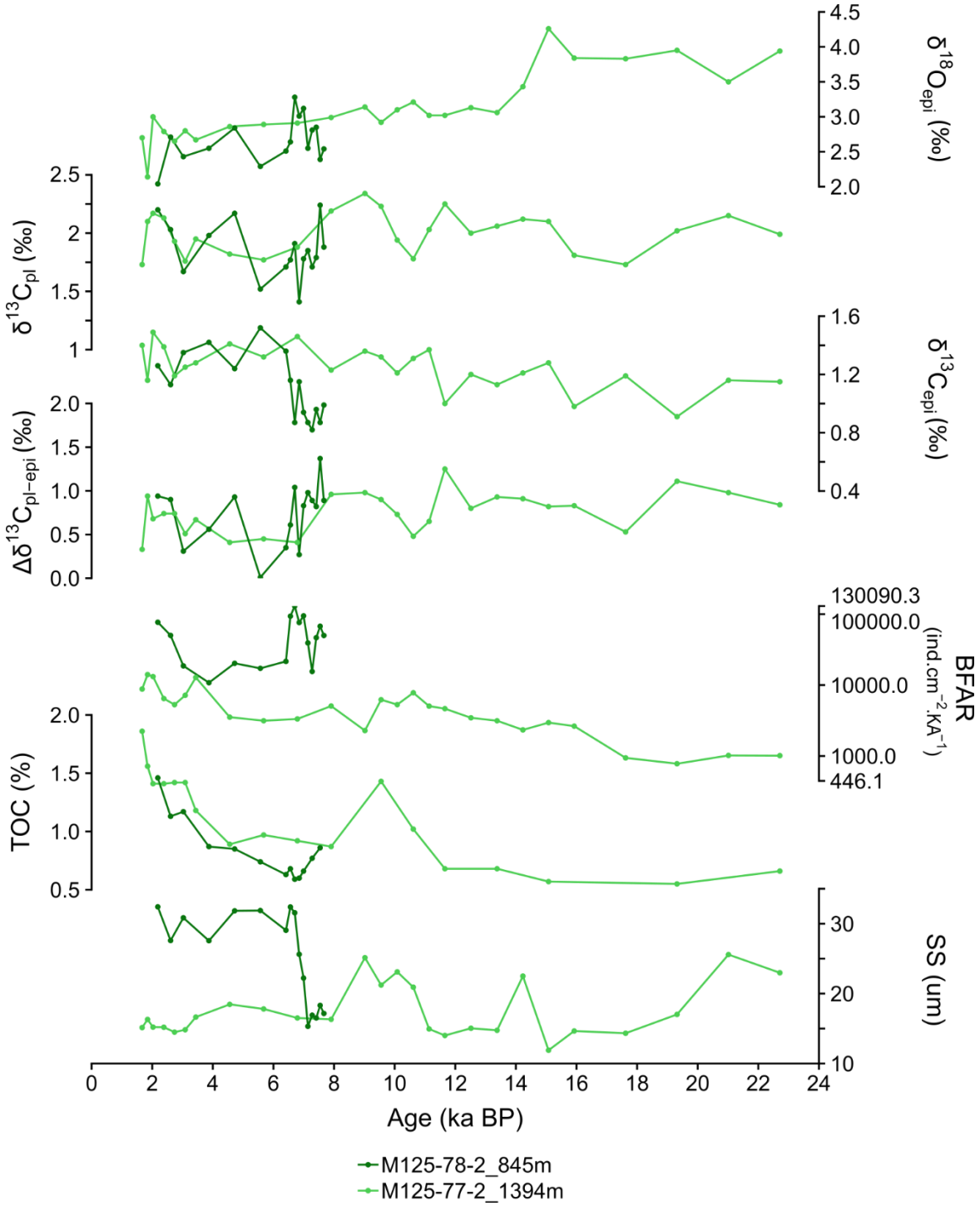

CAPTION: Comparison between $\delta^{18}O_{epi}$, $\delta^{13}C_{pl}$, $\delta^{13}C_{epi}$, $\Delta\delta^{13}C_{pl\text{-}epi}$, TOC and BFAR and sortable silt from cores M125-78-2 (dark green) and M125-77-2 (light green). Note the $\delta^{18}O_{epi}$ scale is inverted
SOURCE: Prepared by the author, 2020.

7 DISCUSSION

7.1 Benthic foraminifera $\delta^{13}C$ viability as AAIW $\delta^{13}C_{DIC}$ proxy

Benthic foraminifera tests $\delta^{13}C$ is considered a good proxy for the $\delta^{13}C_{DIC}$ reconstruction (MACKENSEN, 2004; KATZ et al., 2010) and has been long used as a tracer for water mass and deep-water circulation (MACKENSEN et al., 1993; CURRY; OPPO, 2005). However, the $\delta^{13}C$ records of epibenthic foraminifera might be also sensible to fractionation by other phenomena, such as phytodetritus deposition, thermodynamically driven exchange of carbon isotopes, and vital effects in the foraminifera (BROECKER; MAIER-REIMER, 1992; MACKENSEN et al., 1993; LYNCH-STIEGLITZ et al., 1995; HERTZBERG et al., 2016). A comparison between $\delta^{13}C_{epi}$ and $\delta^{18}O_{epi}$ reveals that the latter does not varies as much as the former along both cores (Figure 9), therefore the shifts in the $\delta^{13}C_{epi}$ probably are not related to a change in the local parameters (temperature, salinity) of the water mass, because if that was the case a matching alteration on $\delta^{18}O_{epi}$ would be expected, but instead are due to changes in the $\delta^{13}C_{DIC}$.

So, we proceeded to analyze the possibility of phytodetrital influence in our study region. To evaluate the reliability of our $\delta^{13}C_{epi}$ in reflecting the $\delta^{13}C_{DIC}$, we compared the data from our cores with other three AAIW-bathed cores from similar depths in the southwestern Atlantic: KNR159-5-36GGC (27.5°S, 46.5°W, 1268m; UMLING et al., 2019), KNR159-5-90GGC (27.35°S, 46.63°W, 1108m; UMLING et al., 2019), and GeoB2107-3 (27.17°S, 46.45°W, 1048m; PORTILHO-RAMOS et al., 2018) (Figures 4, 6 and 9). All five cores $\delta^{13}C_{epi}$ show a similar value range for the deglacial and Holocene (Figure 10). Core M125-77-2 has a higher value than the other cores during the deglacial, but this is probably due to its position in the transition zone between AAIW and NADW, since the latter has higher $\delta^{13}C_{DIC}$ values (CURRY; OPPO, 2005) (Figures 6 and 10).

Figure 10 - Benthic foraminifera δ13C comparison

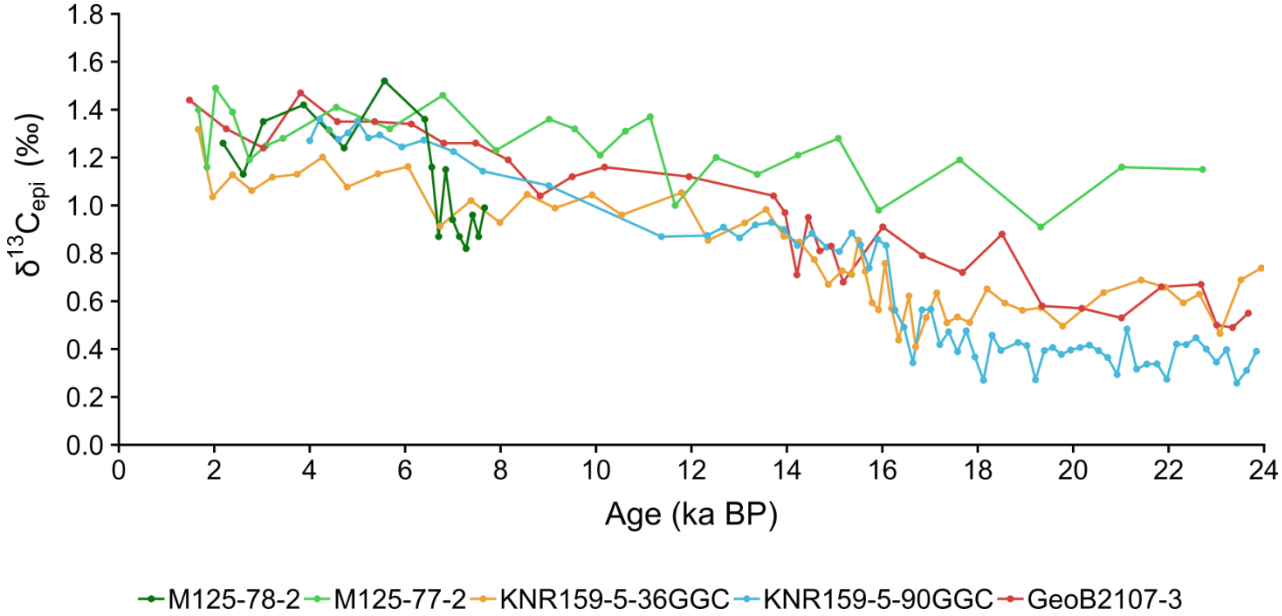

CAPTION: Benthic foraminifera $\delta^{13}C$ comparison for cores M125-78-2 (dark green), M125-77-2 (light green), KNR159-5-36GGC (yellow, UMLING et al., 2019), KNR159-5-90GGC (light blue, UMLING et al., 2019) and GeoB2107-3 (red, PORTILHO-RAMOS et al., 2018).
SOURCE: Prepared by the author, 2020.

A reduction in the carbon exportation due to paleoproductivity changes at the study region in the Holocene also could increase the $\delta^{13}C_{epi}$ but would have the opposite effect on the planktonic foraminifera $\delta^{13}C$ (MACKENSEN et al., 1993). There is a small decrease in the $\delta^{13}C_{pl}$ values during the mid-Holocene for both cores, however $\delta^{13}C_{pl}$ shows an approximately 0.25‰ reduction, while $\delta^{13}C_{epi}$ values were about 0.5‰ higher (Figure 9).

Furthermore, it would be expected a decrease in the BFAR, as reduced carbon exportation decreases the amount of food available in the sediments to be consumed by benthic fauna, thus decreasing the accumulation of benthic foraminifera, but instead, we detected the highest BFAR values in core M125-78-2, which is not consistent with the $\delta^{13}C_{epi}$ high values (Figure 9).

A reduction in TOC would also be expected in case of reduced carbon exportation, but although core M125-78-2 does show a small reduction in the TOC percentage during the mid-Holocene, core M125-77-2 does not show a significant change (Figure 9). Therefore, the increase of epifaunal benthic foraminifera $\delta^{13}C$ in the

mid-Holocene does not represent a reduction in the carbon exportation in relation to the deglacial period.

Our data suggests that the shift in $\delta^{13}C_{epi}$ toward higher values in core M125-78-2 after 8ka was due to changes in the water mass $\delta^{13}C_{DIC}$. This increase in the $\delta^{13}C$ of AAIW may be explained by three hypotheses: 1) air-sea exchange in the formation area of the water mass, due to a surface temperature reduction; 2) a decrease in productivity in the formation area of AAIW or along its flow path, lowering the amount of light carbon isotope exported to intermediate depths; or 3) increased intensity and ventilation of the water mass.

Thermodynamic exchange of carbon isotopes between the atmosphere and surface ocean was the first mechanism that could be affecting our $\delta^{13}C_{epi}$ signal. In thermodynamic equilibrium conditions, the temperature affects the water in such way that it becomes more enriched in ^{13}C as it cools and vice-versa, so that the temperature-driven ^{13}C exchange between atmospheric CO_2 and the surface ocean CO_2 can be calculated, and it was estimated by Broecker and Maier-Reimer (1992) as being about 1‰ enrichment/depletion in ^{13}C for a 10°C decrease/increase in water temperature. Consequently, a cooling in the AAIW formation site could have an impact in the signal. Applying this calculation to our cores, we observe a variation of approximately 0.5‰ in core M125-78-2, which by this slope would mean a 5°C lowering in temperature, considering that most of the change was driven by temperature change. In a study with ice cores from Antarctica, Masson et al. (2000) identified Holocene climatic fluctuations, from a thermal optimum (11.5 to 9ka), to a thermal minimum (at about 8ka), and their findings suggest an ~2°C temperature change between these events. Even if this temperature change in continental Antarctica was completely reflected at the sea surface temperature, this would result in an approximate 0.2‰ change, which alone is not enough to account for the ~0.5‰ variation in $\delta^{13}C_{epi}$ observed. Also, the SS shift indicates an increase in bottom current velocities, but ocean cooling alone cannot explain this increase with the same timing as the $\delta^{13}C_{epi}$.Thus, the possibility of Southern Ocean cooling was discarded as the main cause for $\delta^{13}C_{epi}$ high value.

The second hypothesis for the $\delta^{13}C_{DIC}$ change of the AAIW is a decrease in productivity in the formation region, which would lead to less ^{12}C carbon-rich organic matter export to the intermediate depths, and to evaluate that we compared our data

with paleoproductivity proxies. Opal flux can be used as a surface ocean productivity proxy, since biogenic opal is produced mainly by diatoms – phytoplankton primary producers (CHARLES et al., 1991). Opal flux data from the Southern Ocean (Anderson et al., 2009) does not show indications of enhanced productivity in the Atlantic sector during mid-Holocene.

Another proxy for paleoproductivity is the cadmium of seawater (Cd_w), that has a positive correlation with the nutrient content because organisms are highly efficient in uptaking Cd – a micronutrient - from the surface ocean (BOYLE, 1988; RICKABY; ELDERFIELD, 2005). As such, surface Cd_W and $\delta^{13}C_{DIC}$ of intermediate waters have a negative relationship, because as organisms take nutrients and light carbon from the surface and export them to intermediate/deep ocean, surface Cd_w lowers while the $\delta^{13}C_{DIC}$ of intermediate waters increases, hence, the Cd/Ca ratio from benthic foraminifera tests can be used to estimate the Cd_W and, thus, the paleoproductivity (BOYLE, 1988; MACKENSEN, 2004; POGGEMANN et al., 2017; UMLING et al., 2019). We compared our data with Cd_w data from two cores bathed by the AAIW, and thus the Cd_w are related to the paleoproductivity variation at the AAIW formation region in the Southern Ocean.

Cd_w data from core M78/1-235-1, collected at the Tobago Basin in the western tropical Atlantic at about 850m depth, does not point toward a decrease in productivity at the AAIW formation site, since the values do not reveal a decrease during the mid-Holocene (POGGEMANN et al., 2017) (Figure 11). Data of Cd_w from core KNR159-5-90GGC (UMLING et al., 2019), similarly, do not indicate a decrease in the nutrient content of AAIW at the time, in good agreement with the opal flux data (ANDERSON et al., 2009). Hence, the enrichment in benthic foraminifera $\delta^{13}C$ from core M128-78-2 was not due to variations in paleoproductivity in the Atlantic subpolar front.

Figure 11 - Data comparison between both cores of this study and other AAIW-bathed cores

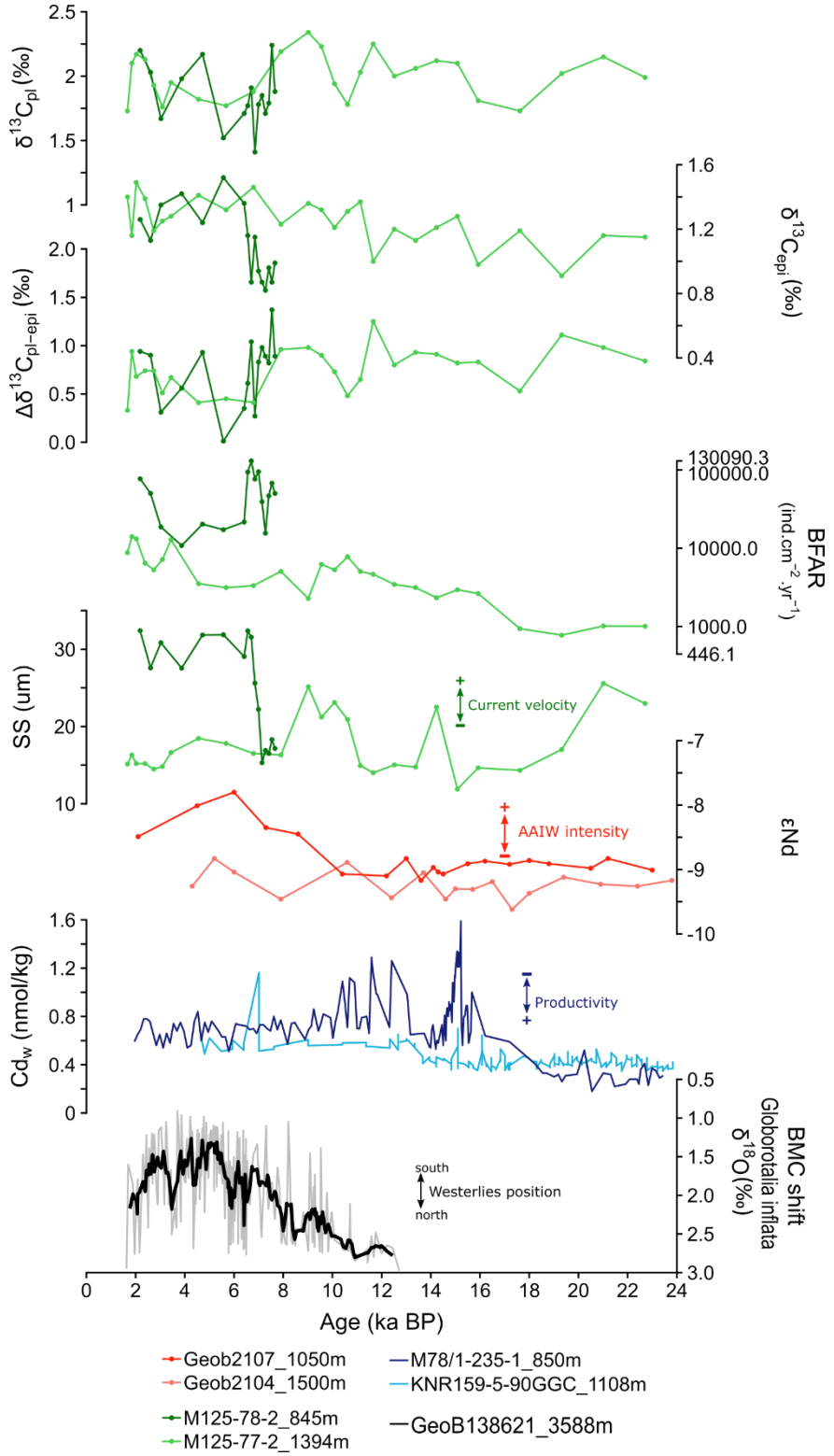

CAPTION: Comparison between $\delta^{13}C_{epi}$, $\Delta\delta^{13}C_{pl\text{-}epi}$, BFAR and sortable silt from cores M125-78-2 and M125-77-2 (this study), εNd data from cores Geob2107 and Geob2104 (HOWE et al., 2016), and Cd_w data from cores M78/1-235-1 (POGGEMANN et al., 2017) and KNR159-5-90GGC (UMLING et al., 2019), and BMC shift proxy data from core GeoB138621 (VOIGT et al., 2015).
SOURCE: Prepared by the author, 2020.

To assess the hypothesis of intensification of the AAIW flow during the mid-Holocene, we used bottom current velocity-proxy sortable silt and published εNd values. The εNd value of a water mass is related to the continental weathering around the formation site, in a way that older/younger rocks imprint a less/more radiogenic signal, and is used as a quasi-conservative tracer of ocean circulation and mixing (FRIEDRICH et al., 2014). NADW has less radiogenic εNd values, while Pacific formed-water masses display more radiogenic values, and AAIW show an intermediate value of ~8.5 (FRIEDRICH et al., 2014; HOWE et al., 2016).

Comparison with εNd values from core GeoB2107-3 (HOWE et al., 2016), located at 1050m water depth in the southwestern Atlantic, show a similarity in timing between the excursion towards more radiogenic values of AAIW and the sharp rise in sortable silt data from core M125-78-2, pointing toward an increase in velocity of the AAIW flow at 850m depth (Figure 11). Core M125-77-2, at 1400m depth, however, does not show the same variation for the Holocene. It is positioned within the mixing layer between AAIW and NADW, and sortable silt values are more comparable with the GeoB2104-3 εNd data (HOWE et al., 2016), collected at 1500m depth, which does not show great variations along the Holocene. We interpret that the mixing ratio between AAIW and NADW did not change sensibly at this depth, despite variations of these water masses intensities.

Therefore, we argue that the increase in $\delta^{13}C_{epi}$ detected in core M125-78-2 data during the mid-Holocene is due to an intensification of AAIW circulation. Sortable silt data indicate an increase in flow velocity, but the position of the core M125-77-2 within the mixing layer between AAIW and NADW did not allow us to detect changes in the water mass volume (Figures 4 and 5). Enhanced intensity of the AAIW would increase ventilation of the water mass, diminishing the time to accumulate carbon and, thus, the amount of ^{13}C-depleted CO_2 accumulated from vertically transported organic matter along its path until it reached our core site. Some mechanisms have been proposed to explain the apparent intensification of AAIW during mid-Holocene. There is also evidence for an increase in the vertical extension of AAIW, and consequently in volume, associated with the intensification in mid-Holocene (HOWE et al., 2016; VOIGT et al., 2016), but core M125-77-2, at ~1400m depth, does not record significant changes in the mid-Holocene, probably because of its depth. It is possible that the

mixing between AAIW and NADW at this depth was constant over the Holocene and we cannot detect the variations in AAIW flow.

7.2 $\Delta\delta^{13}C$ as evidence for a wind-driven AAIW intensity increase

Not only do the $\delta^{13}C_{epi}$ and SS proxies show a variation in the mid-Holocene, but also the $\Delta\delta^{13}C_{pl\text{-}epi}$ reveals a comparable timing with the εNd values from GeoB2107-3. Our reconstruction is coherent with that from Hertzberg et al. (2016), which also detect a decrease in $\Delta\delta^{13}C_{pl\text{-}epi}$ around 8ka in the southwestern Atlantic (Figures 11 and 12). Even though our reconstruction allow us to identify clear variations of the $\Delta\delta^{13}C_{pl\text{-}epi}$ during the Holocene, this variability is not connected to changes in the biological pump in the Southern Ocean, as revealed from the lack of alteration of Cd_w and opal flux proxies in the mid-Holocene (ANDERSON et al., 2009; POGGEMANN et al., 2017; UMLING et al., 2019) (Figure 11).

The decrease in the $\Delta\delta^{13}C_{pl\text{-}epi}$ could also be due to a weakening of the local productivity during the mid-Holocene, which is not observed, as discussed in session 5.1, because for the increase in $\delta^{13}C_{epi}$ it would be expected a similar reduction in $\delta^{13}C_{pl}$ values (Figures 7 and 10). The $\delta^{13}C$ gradient is also in disagree with the BFAR index, which showed a sharp increase in core M125-78-2, where the contrary would be expected in case of decreasing local organic carbon exportation (Figure 7 and 10). Hence, we propose that the $\Delta\delta^{13}C_{pl\text{-}epi}$ is reflecting neither changes in productivity at the study region nor at the AAIW formation area during the mid-Holocene, rather, it is showing the intensity changes of AAIW. The altered AAIW $\delta^{13}C_{DIC}$ increases the $\delta^{13}C_{epi}$, thus modifying the $\delta^{13}C$ gradient even without any vertical carbon transport change.

Hertzberg et al. (2016) analyzed surface-intermediate waters $\Delta\delta^{13}C$ for four cores from different sites: the Brazilian margin, Cathan Rise, Australian margin and eastern equatorial Pacific (Figure 12). The $\Delta\delta^{13}C$ data shows that the Brazilian margin gradient has a distinct decreasing pattern during the mid-Holocene, which is not observed in the $\Delta\delta^{13}C$ for the Southern Ocean, South Pacific and Eastern Equatorial Pacific data (HERTZBERG et al.; 2016) (Figure 12). Therefore, we argue that the difference observed between the Southwestern Atlantic and the other oceanic basins $\Delta\delta^{13}C$ is not only due to productivity variations but also due to changes in the regional intermediate water dynamics. More intense intermediate water circulation could

account for the rise in $\delta^{13}C_{epi}$ observed during mid-Holocene (~+0.25‰ in relation to the $\delta^{13}C_{pl}$ decrease, see session 7.1), and thus explain the $\delta^{13}C$ gradient decoupling from the productivity.

As a result of its sensibility to water mass dynamics change, $\Delta\delta^{13}C$ could not be used as a reliable paleoproductivity proxy in the Southwestern Atlantic during the mid-Holocene. Its use require attention to intermediate water variability and verification from other paleoproductivity proxies.

Figure 12 - Records of $\delta^{13}C$ (planktonic and benthic foraminifera) and $\Delta\delta^{13}C$ across the deglaciation

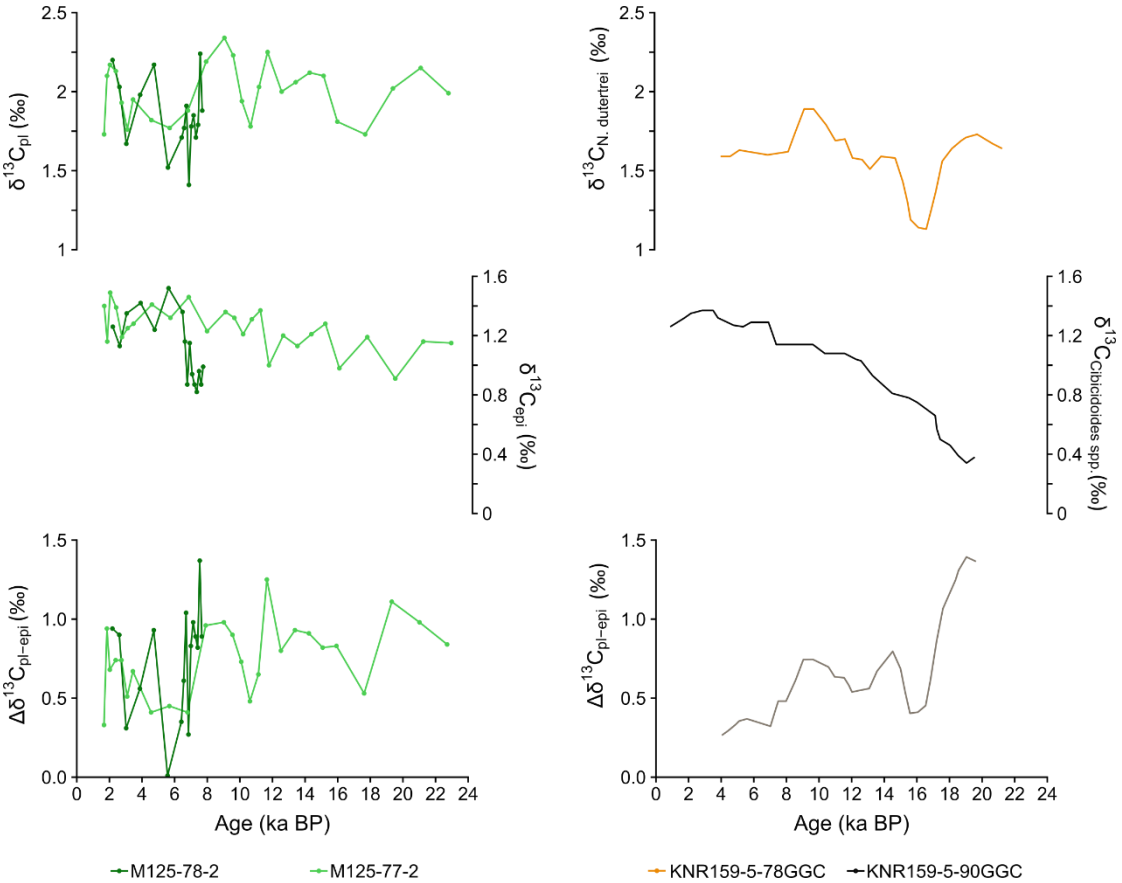

CAPTION: comparison between planktonic and benthic $\delta^{13}C$ and $\Delta\delta^{13}C$ records from cores: M125-78-2 (dark green; this study), M125-77-2 (light green; this study), KNR159-5-78GGC (orange; 2kyr running mean; HERTZBERG et al., 2016), and KNR159-5-90GGC (black; 2kyr running mean; CURRY; OPPO, 2005, in HERTZBERG et al., 2016). Gray line represents the calculated $\Delta\delta^{13}C$ between *Neogloboquadrina dutertrei* (orange) and *Cibicidoides spp.* (black) $\delta^{13}C$ data (2kyr running mean; HERTZBERG et al., 2016).
SOURCE: prepared by the author, 2020. Cores KNR159-5-78GGC and KNR159-5-90GGC data from HERTZBERG et al.; 2016

Voigt et al. (2016) have also found sortable silt evidence for strengthened AAIW circulation in the southwestern Atlantic around 7ka. In their study, they argue that the intensification of AAIW has strong correlation with the Holocene climatic fluctuations and is in antiphase with NADW strength (Voigt et al., 2016, and references therein). However, an intensification of AMOC during the mid-Holocene is still unclear since results are contradictory. A study using model simulations points toward stronger AAIW and weaker NADW production (WAINER et al., 2012), while another with Pa/Th and εNd data suggest stronger NADW production in the mid-Holocene (LIPPOLD et al., 2016). There is also recent evidence from Pa/Th at the Equatorial Atlantic indicating no variation in NADW production (LIPPOLD et al., 2019). Therefore, whether a stronger AAIW production is in anyway related to the NADW production or not is uncertain. Furthermore, the relation between Holocene Antarctic climatic fluctuations and AAIW variation is not supported by our data. The $\delta^{13}C_{epi}$ Holocene variation in core M125-78-2 is of ~0.5‰, which, accordingly to the slope calculated by Broecker and Maier-Reimer (1992), would mean a 5°C cooling in the Southern Ocean, for what there is no evidence, as discussed in session 5.1.

Howe et al. (2016) hypothesized that the more radiogenic values in the mid-Holocene could be due to stronger AAIW production and/or to an increased proportion of more radiogenic Pacific waters in its composition, which would have been caused by a southward shift in the position of the westerly winds. Voigt et al. (2016), however, rejects this hypothesis because the timing of the westerlies shift (~5ka) does not coincide with the strengthening of AAIW (~7ka). Then, we compared our data with that from Voigt et al. (2015), which uses the $\delta^{18}O$ values from planktonic foraminifera *Globorotalia inflata* as a proxy for the position of the Brazil Malvinas Confluence (BMC) (Figure 10). The latitudinal variation of the BMC is influenced by the displacement of the south westerlies wind stress (Voigt et al., 2015, and references therein). The onset of a southward displacement of the westerlies in the mid-Holocene is coherent in timing with the shift in our $\Delta\delta^{13}C$, $\delta^{13}C_{epi}$ and SS data for core M125-78-2 (Figure 11).

Studies show that the intensity of the Antarctic Circumpolar Current (ACC) is strongly dependent on the southern westerly winds, and that a southward shift of this wind belt during interglacial periods increased the transportation of water from the Pacific into the Atlantic through the Drake Passage (VOLKER & KÖHLER, 2013; LAMY et al., 2015). AAIW is formed in the Southwest Pacific and a part of the water mass

enter the Pacific Gyre, while another fraction pass to the South Atlantic (GORDON, 1986; LAMY et al., 2015).

Thus, we hypothesize that a southward shift of the southern westerly winds in the mid-Holocene led to enhanced transport of AAIW from the Pacific to the Atlantic through the Drake Passage. The more radiogenic Pacific waters and greater amount of AAIW flowing northwards would be responsible for the shift towards more radiogenic εNd values and increased intensity of water mass flow reflected in the SS and carbon isotopes data.

8 CONCLUSIONS

Stable isotope and granulometry analyses revealed a change in the intermediate water dynamics in the mid-Holocene. Our intermediate-depth core M125-78-2 core shows a strong shift in most variables around 8 ka BP, which is not reflected in core M125-77-2 data. The increase in $\delta^{13}C$ from benthic foraminifera and the increase in the sortable silt fraction of the sediment are compatible with the hypothesis for an intensification of AAIW during the mid-Holocene.

Our data also supports that AAIW dynamics has decoupled the $\delta^{13}C$ gradient from the biological pump mechanism. Differently from the observed for the deglaciation, the decrease in $\Delta\delta^{13}C_{pl\text{-}epi}$ in the same timing then the SS and $\delta^{13}C$ reveals that this proxy is not reflecting the effectiveness of the biological pump, but rather is also sensible to variations in the intensity of circulation. Increased AAIW circulation in the Southwestern Atlantic has increased the benthic foraminifera $\delta^{13}C$, yielding a decrease in the $\delta^{13}C$ gradient.

Although the mechanisms behind the strong AAIW circulation during mid-Holocene are still unclear, our data do not support a relation to the NADW formation and the AMOC intensification in mid-Holocene. The most acceptable mechanism could be the southward shift of westerly winds which led to enhanced transport of AAIW from the Pacific to the Atlantic through the Drake Passage. M125-77-2 core position within the mixing layer does not allow us to detect vertical expansion of AAIW during the mid-Holocene, even though there is evidence for volume change from a previous study. These mid-Holocene shifts in intermediate circulation, especially in regard to the enhanced Drake Passage flow, are of great importance for AMOC fluctuations, since the Pacific-sourced intermediate water is of lower temperature and salinity than that coming from the Agulhas leakage, thus having a great potential of playing an important role in the weakening and re-establishment of the Atlantic circulation. Thus, improved knowledge about the AAIW variation causes will allow to better forecast future ocean circulation patterns and its effects.

9 REFERENCES

ANDERSON, R. F.; ALI, S.; BRADTMILLER, L. I.; NIELSEN, S. H. H.; FLEISHER, M. Q.; ANDERSON, B. E.; BURCKLE, L. H. Wind-Driven Upwelling in the Southern Ocean and the Deglacial Rise in Atmospheric CO_2. **Science**, v. 323, p. 1443-1448, 2009. DOI: 10.1126/science.1167441

BERGER, A.; MÉLICE, J. L. and LOUTRE, M. F. On the origin of the 100-kyr cycles in the astronomical forcing, **Paleoceanography**, v. 20, n. 4, 2005. DOI: 10.1029/2005PA001173.

BALMER, S.; SARNTHEIN, M.; MUDELSEE, M. and GROOTES, P. M. Refined modeling and 14C plateau tuning reveal consistent patterns of glacial and deglacial ^{14}C reservoir ages of surface waters in low‐latitude Atlantic, **Paleoceanography**, v. 31, p.1030–1040, 2016. DOI:10.1002/2016PA002953.

BLAAUW, M.; CHRISTEN, J. A. Flexible paleoclimate age-depth models using an autoregressive gamma process. **Bayesian Analysis**, v. 6, n. 3, p. 457–474, 2011. DOI: 10.1214/11-BA618

BLUNIER, T.; BROOK, E. J. Timing of Millennial-Scale Climate Change in Antarctica and Greenland During the Last Glacial Period. **Science**, v. 291, p. 109-112, 2001. DOI: 10.1126/science.291.5501.109

BOEBEL, O.; DAVIS, R. E.; OLLITRAULT, M.; PETERSON, R. G.; RICHARDSON, P. L.; SCHMID, C.; ZENK, W. The intermediate depth circulation of the western South Atlantic. **Geophysical Research Letters**, American Geophysical Union, v. 26, n. 21, p. 3329–3332, 1999. DOI: 10.1029/1999GL002355.

BOHM, E.; LIPPOLD, J.; GUTJAHR, M.; FRANK, M.; BLASER, P.; ANTZ, B.; FOHLMEISTER, J.; FRANK, N.; ANDERSEN, M. B.; DEININGER, M. Strong and deep Atlantic meridional overturning circulation during the last glacial cycle. **Nature**, v. 517, n. 7532, p. 73–76, 2015. DOI: 10.1038/nature14059

BOLTOVSKOY, E.; WRIGHT, R. C. **Recent Foraminifera**. [S.l.]: Springer Science & Business Media, 2013. 515 p.

BOUDAGHER-FADEL, M. K. (Ed.) **An introduction to planktonic foraminifera**: Developments in Palaeontology and Stratigraphy. 2. Ed. London: UCLPRESS, 2012. 310p. DOI: 10.1016/B978-0-444-53638-9.00001-5

BOYER, T.P.; ANTONOV, J. I.; BARANOVA, O. K.; COLEMAN, C.; GARCIA, H. E.; GRODSKY, A.; JOHNSON, D. R.; LOCARNINI, R. A.; MISHONOV, A. V.; O'BRIEN, T.D.; PAVER, C.R.; REAGAN, J.R.; SEIDOV, D.; SMOLYAR, I. V.; ZWENG, M. M. World Ocean Database 2013. In: S. Levitus; A. Mishonov (Eds.). **NOAA Atlas NESDIS 72**. Silver Spring, MD, 2013. 209 p. DOI: 10.7289/V5NZ85MT

BOYLE, E. A. Cadmium: Chemical tracer of deepwater paleoceanography. **Paleoceanography**, v. 3, n. 4, p. 471–489, 1988. DOI:10.1029/pa003i004p00471

BROECKER, W. S. & MAIER-REIMER, E. The influence of air and sea exchange on the carbon isotope distribution in the sea. **Global Biogeochemical Cycles**, v. 6, p. 315–320, 1992. DOI:10.1029/92GB01672

BROECKER, W.S. Massive iceberg discharges as triggers for global climate change. **Nature**, v. 372, p. 421-424, 1994.

BROECKER, W. S. Paleocean circulation during the last deglaciation: A bipolar seesaw? **Paleoceanography**, v. 13, n. 2, p. 119–121, 1998. DOI: 10.1029/97PA03707.

BURDIGE, D.J. Preservation of Organic Matter in Marine Sediments: Controls, Mechanisms, and an Imbalance in Sediment Organic Carbon Budgets? **Chemical Reviews**, v. 107, n. 2, 2007. DOI: 10.1021/cr050347q

CHARLES, C. D.; FROELICH, P. N.; ZIBELLO, M. A.; MORTLOCK, R. A.; MORLEY, J. J. Biogenic opal in Southern Ocean sediments over the last 450,000 years: Implications for surface water chemistry and circulation. **Paleoceanography**, v. 6, n. 6, p. 697–728, 1991. DOI:10.1029/91pa02477

CURRY, W. B.; OPPO D. W. Glacial water mass geometry and the distribution of $d^{13}C$ of $\sum CO_2$ in the western Atlantic Ocean. **Paleoceanography**, v. 20, p. 1-13, 2005. DOI:10.1029/2004PA001021

GARABATO, N.A.C.; JULLION, L.; STEVENS, D.P.; HEYWOOD, K.J.; KING, B.A. Variability of subantarctic mode water and Antarctic Intermediate Water in the Drake Passage during the late-twentieth and early-twenty-first centuries. **Journal of Climate**, v. 22, n. 13, p. 3661–3688, 2009. DOI: 10.1175/2009JCLI2621.1

GOLSTEIN, S. T. Foraminifera: a biological overview. In: GUPTA, B. K. S. **Modern Foraminifera**. Dordrecht: Springer, 1999. p. 37-55. DOI:10.1007/0-306-48104-9_3

GORDON, A. L. Interocean exchange of thermocline water. **Journal of Geophysical Research**, v. 91, n. C4, p. 5037-5046, 1986. DOI: 10.1029/jc091ic04p05037.

HEINRICH, H. Origin and Consequences of Cyclic Ice Rafting in the Northeast Atlantic Ocean During the Past 130,000 Years. **Quaternary Research**, v. 29, n. 2, p. 142–152, 1988. DOI: 10.1016/0033-5894(88)90057-9.

HENDRY, K. R.; ROBINSON, L. F.; MEREDITH, M. P.; MULITZA, S.; CHIESSI, C. M.; ARZ, H. Abrupt changes in high-latitude nutrient supply to the Atlantic during the last glacial cycle. **Geology**, v. 40, p. 123-126, 2012. DOI: 10.1130/G32779.1

HERGUERA, J. C.; BERGER, W. H. Paleoproductivity from benthic foraminifera abundance: Glacial to postglacial change in the west-equatorial Pacific. **Geology**, v. 19, n. 12, p. 1173-1176, 1991.

HERTZBERG, J. E.; LUND, D. C.; SCHMITTNER, A.; SKRIVANEK, A. L. Evidence for a biological pump driver of atmospheric CO_2 rise during Heinrich Stadial 1. **Geophysical Research Letters**, v. 43, 2016. DOI:10.1002/2016GL070723.

HILBRECHT, H. Morphologic gradation and ecology in *Neogloboquadrina pachyderma* and *N. dutertrei* (planktic foraminifera) from core top sediments. **Marine Micropaleontology**, v. 31, p. 31–43, 1997. DOI: 10.1016/S0377-8398(96)00054-0

HOWE, J. N. W.; PIOTROWSKI, A. M.; OPPO, D. W.; HUANG, K.F.; MULITZA, S.; CHIESSI, C. M.; BLUSZTAJN, J. Antarctic intermediate water circulation in the South Atlantic over the past 25000 years. **Paleoceanography**, v. 31, p. 1302–1314, 2016. DOI: 10.1002/2016PA002975

HUANG, K. F., OPPO, D. W.; CURRY, W. B. Decreased influence of Antarctic intermediate water in the tropical Atlantic during North Atlantic cold events. **Earth and Planetary Science Letters**, v. 389, p. 200–208, 2014. DOI: 10.1016/j.epsl.2013.12.037

IPCC. **Climate Change 2013**: The Physical Science Basis. Cambridge, United Kingdom and New York, NY, USA: Cambridge University Press, 2013. 1535 p. Disponível em: < https://www.ipcc.ch/report/ar5/wg1/>. Acesso em: 11 fev. 2020.

IPCC. **Climate Change 2014**: Synthesis Report. Geneva, Switzerland, 2014. 151p. Disponível em: <https://www.ipcc.ch/report/ar5/syr/>. Acesso em: 31 jan. 2018.

JONES, R.W. **The Challenger Foraminifera**. Oxford: Oxford University Press, 1994. 149p.

KATZ, M.; CRAMER, B.; FRANZESE, A.; HONISCH, B.; MILLER, K.; ROSENTHAL, Y.; WRIGHT, J. Traditional and emerging geochemical proxies in foraminifera. **The Journal of Foraminiferal Research**, v. 40, n. 2, p. 165-192, 2010.

LAMY, F.; KILIAN, R.; ARZ, H. W.; FRANCOIS, J.P.; KAISER, J.; PRANGE, M. Glacial reduction and millennial-scale variations in Drake Passage throughflow. **Proceedings of the National Academy of Sciences of the United States of America**, v. 112, n. 44, p. 13496–13501, 2015. DOI: 10.1073/pnas.1509203112.

LIPPOLD, J.; GUTJAHR, M.; BLASER, P.; CHRISTNER, E.; FERREIRA, M. L. C.; MULITZA, S.; CHRISTL, M.; WOMBACHER, F.; BÖHM, E.; ANTZ, B.; CARTAPANIS, O.; VOGEL, H.; JACCARD, S. L. Deep water provenience and dynamics of the (de)glacial Atlantic meridional overturning circulation. **Earth and Planetary Science Letters**, v. 445, p. 68–78, 2016. DOI: 10.1016/j.epsl.2016.04.013

LOEBLICH, A.; TAPPAN, H. **Foraminiferal Genera and their Classification**. New York: Van Nostrand Reinhold Company, 1988. 970 p.

LYNCH‐STIEGLITZ, J.; STOCKER, T. F.; BROECKER, W. S.; FAIRBANKS, R. G. The influence of air-sea exchange on the isotopic composition of oceanic carbon:

Observations and modeling. **Global Biogeochemical Cycles**, v. 9, n. 4, p. 653–665, 1995. DOI: 10.1029/95GB02574

MACAYEAL, D. R. Binge/purge oscillations of the Laurentide Ice Sheet as a cause of the North Atlantic's Heinrich events. **Paleoceanography**, v. 8, n.6, p. 775–784, 1993. DOI: 10.1029/93PA02200

MCCAVE, I.; MANIGHETTI, B.; ROBINSON, S. Sortable silt and fine sediment size/composition slicing: parameters for palaeocurrent speed and palaeoceanography. **Paleoceanography**, v. 10, n. 3, p. 593–610, 1995.

MCCAVE, I. N. Size sorting during transport and deposition of fine sediments: Sortable silt and flow speed. In: **Contourites,** Developments in Sedimentology, v. 60. Amsterdam: Elsevier, 2008. p. 121-142. ISBN 978-0-444-52998-5. DOI: 10.1016/S0070-4571(08)10008-5

MACKENSEN, A.; HUBBERTEN, H.-W.; BICKERT, T.; FISCHER, G.; FÜTTERER, D.K. The $\delta^{13}C$ in benthic foraminiferal tests of *Fontbotia wuellerstorfi* (Schwager) relative to the $\delta^{13}C$ of dissolved inorganic carbon in Southern Ocean deep water: Implications for glacial ocean circulation models. **Paleoceanography**, v. 8, p. 587–610, 1993.

MACKENSEN, A. Changing Southern Ocean palaeocirculation and effects on global climate. **Antarctic Science**, v. 16, n. 4, p. 369–386, 2004. DOI: 10.1017/S0954102004002202

MCMANUS, J. F.; OPPO, D. W.; CULLEN, J. L. A 0.5-Million-Year Record of Millennial-Scale Climate Variability in the North Atlantic. **Science**, v. 283, p. 971-975, 1999.

MCMANUS, J. F.; FRANCOIS, R; GHERARDL, J. M.; KELGWIN, L.; DROWN-LEGER, S. Collapse and rapid resumption of Atlantic meridional circulation linked to deglacial climate changes. **Nature**, v. 428, n. 6985, p. 834–837, 2004. DOI: 10.1038/nature02494

MARTINS, L. R.; COUTINHO, P. N. The Brazilian continental margin. **Earth-Science Reviews**, v. 17, p.87–107, 1981. DOI:10.1016/0012-8252(81)90007-6

MASSON, V.; VIMEUX, F.; JOUZEL, J.; MORGAN, V.; DELMOTTE, M; CIAIS, P.; HAMMER, C.; JOHNSEN, S.; LIPENKOV, V.Y.; MOSLEY-THOMPSON, E.; PETIT, J-R.; STEIG, E.J.; STIEVENARD, M.; VAIKMAE, R. Holocene climate variability in Antarctica based on 11 ice-core isotopic records. **Quaternary Research**, v. 54, n. 3, p. 348–358, 2000. DOI: 10.1006/qres.2000.2172.

PAHNKE, K.; ZAHN, R. Southern Hemisphere water mass conversion linked with North Atlantic climate variability. **Science**, v. 307, p. 1741–1746, 2005. DOI: 10.1126/science.1102163

PAHNKE, K.; GOLDSTEIN, S.L.; HEMMING, S.R. Abrupt changes in Antarctic Intermediate Water circulation over the past 25,000 years. **Nature Geoscience**, v. 1, p. 870-874, 2008. DOI:10.1038/ngeo360

POGGEMANN, D.W.; HATHORNE, E. C.; NÜRNBERG, D.; FRANK, M.; BRUHN, I.; REIßIG, S.; BAHR, A. Rapid deglacial injection of nutrients into the tropical Atlantic via Antarctic Intermediate Water. **Earth and Planetary Science Letters**, v. 463, p. 118-126, 2017. DOI: 10.1016/j.epsl.2017.01.030.

RAHMSTORF, S. Ocean circulation and climate during the past 120,000 years', **Nature**, p. 207–214, 2002. DOI: 10.1038/nature01090.

RAHMSTORF, S. Thermohaline Circulation. In: ELIAS, S.A. (Ed.). **Encyclopedia of Quaternary Science**. 2 ed. Amsterdam: Elsevier Science, 2006. p. 737–747. DOI: 10.1016/B978-0-444-53643-3.00020-0.

REIMER, P.J.; BARD, E.; BAYLISS, A.; BECK, J.W.; BLACKWELL, P.G.; BRONK RAMSEY, C.; BUCK, C.E.; EDWARDS, R.L.; FRIEDRICH, M.; GROOTES, P.M.; GUILDERSON, T.P.; HAFLIDASON, H.; HAJDAS, I.; HATTÉ, C.; HEATON, T.J.; HOFFMANN, D.L.; HOGG, A.G.; HUGHEN, K.A.; KAISER, K.F.; KROMER, B.; MANNING, S.W.; NIU, M.; REIMER, R.W.; RICHARDS, D.A.; SCOTT, E.M.; SOUTHON, J.R.; TURNEY, C.S.M.; VAN DER PLICHT, J. IntCal13 and Marine13 radiocarbon age calibration curves, 0-50,000 years cal BP. **Radiocarbon**, v. 55, p. 1869-1887, 2013.

RHEIN, M. Taking a close look at ocean circulation: ocean circulation patterns in the North Atlantic provide a benchmark for climate models. **Science**, v. 363, n. 6426, p. 456-457, 2019.

RICKABY, R. E. M.; ELDERFIELD, H. Evidence from the high-latitude North Atlantic for variations in Antarctic Intermediate water flow during the last deglaciation. **Geochemistry, Geophysics, Geosystems**, v. 6, n. 5, p. 1-12, 2005. DOI: 10.1029/2004GC000858.

RINTOUL, S. R. South Atlantic interbasin exchange. **Journal of Geophysical Research**, v. 96, n.C2, p. 2675–2692, 1991. DOI:10.1029/90jc02422

ROBERTS, J.; MCCAVE, I. N.; MCCLYMONT, E. L.; KENDER, S.; HILLENBRAND, C. D.; MATANO, R.; HODELL, D. A.; PECK, V. L. Deglacial changes in flow and frontal structure through the Drake Passage. **Earth and Planetary Science Letters**, v. 474, p. 397–408, 2017. DOI: 10.1016/J.EPSL.2017.07.004.

RONGE, T. A.; STEPH, S.; TIEDEMANN, R.; PRANGE, M.; MERKEL, U.; NÜRNBERG, D.; KUHN, G. Pushing the boundaries: Glacial/interglacial variability of intermediate and deep waters in the southwest Pacific over the last 350,000 years. **Paleoceanography**, v. 30, p. 23–38, 2015. DOI: 10.1002/2014PA002727

RUDDIMAN, W.F. **Earth's climate**: Past and Future. 3 ed. [S.l.]: W. H. Freeman and Company, 2014. 460p.

RÜHS, S.; SCHWARZKOPF, F. U.; SPEICH, S.; BIASTOCH, A. Cold vs. warm water route-sources for the upper limb of the Atlantic Meridional Overturning Circulation revisited in a high-resolution ocean model. **Ocean Science**, v. 15, n. 3, p. 489–512, 2019. DOI: 10.5194/OS-15-489-2019.

SAENKO, O. A.; WEAVER, A. J.; GREGORY, J. M. On the link between the two modes of the ocean thermohaline circulation and the formation of global-scale water masses. **Journal of Climate**, v. 16, n. 17, p. 2797–2801, 2003. DOI: 10.1175/1520-0442(2003)016<2797:OTLBTT>2.0.CO;2

SCHIEBEL, R.; HEMLEBEN, C. **Planktonic Foraminifers in the Modern Ocean**: Ecology, Biogeochemistry, and Application. 1 ed. Berlin: Springer, 2017. DOI: 10.1007/978-3-662-50297.6

SCHLITZER, R. **Ocean Data View**, odv.awi.de, 2020.

SHARP, Z. **Principles of Stable Isotope Geochemistry**. 1 ed. New Jersey: Pearson Prentice Hall, 2007. 356p. ISBN: 0-13-009139-1

SIGMAN, D.; HAUG, G. The Biological Pump in the Past. In: Holland, H.D. and Turekian, K.K (Eds.). **Treatise on Geochemistry**: The Oceans and Marine Geochemistry. Oxford: Elsevier Pergamon, v. 6, pp. 491-528, 2003. ISBN 0-08-043751-6.

SIGMAN, D.; HAIN, M.; HAUG, G. The polar ocean and glacial cycles in atmospheric CO_2 concentration. **Nature**, v. 466, p. 47–55, 2010.

SILVEIRA, I. C. A.; SCHMIDT, A. K.; CAMPOS, E. J. D.; GODOI, S. S.; e IKEDA, Y. Corrente do Brasil ao Largo da Costa Leste Brasileira. **Revista brasileira de oceanografia**, v. 48, n. 2, p. 171-183, 2000.

SPIEGEL, D. S.; RAYMOND, S. N.; DRESSING, C. D.; SCHARF, C. A.; MITCHELL, J. L. Generalized milankovitch cycles and long-term climatic habitability. **Astrophysical Journal**, v. 721, n. 2, p. 1308–1318, 2010. DOI: 10.1088/0004-637X/721/2/1308.

STRAMMA, L. and ENGLAND, M. On the water masses and mean circulation of the South Atlantic Ocean. **Journal of Geophysical Research:** *Oceans*. American Geophysical Union (AGU), v. 104, n. C9, p. 20863–20883, 1999. DOI: 10.1029/1999jc900139.

TALLEY, L. D. Antarctic Intermediate Water in the South Atlantic. In: WEFER, G., BERGER, W.H., SIEDLER, G., WEBB, D.J (Eds). **The South Atlantic: Present and Past Circulation**. Berlin: Springer, 1996. p. 219–238.

TALLEY, L. D. Some aspects of ocean heat transport by the shallow, intermediate and deep overturning circulations. In: Clark, P. U.; Webb, R. S.; Keigwin, L. D. (Eds.), **Mechanisms of global climate change at millennial time scales**. Washington DC: American Geophysical Union, v. 112; p. 1–22, 1999.

UMLING, N. E.; OPPO, D. W.; CHEN, P.; YU, J.; LIU, Z.; YAN, M.; GEBBIE, G.; LUND, D. C.; PIETRO, K. R.; JIN, Z. D.; HUANG, K.; COSTA, K. B.; TOLEDO, F. A. Atlantic Circulation and Ice Sheet Influences on Upper South Atlantic Temperatures During the Last Deglaciation. **Paleoceanography and Paleoclimatology**, v. 34, p. 990-1005, 2019. DOI:10.1029/2019PA003558.

VIANA, A.R.; FAUGÈRES, J.C.; KOWSMANN, R.O.; LIMA, J.A.M.; CADDAH, L.F.G. Hydrology, morphology and sedimentology of the Campos continental margin, offshore Brazil. **Sedimentary Geology**, v. 115, p. 133-157, 1998.

VOIGT, I.; CHIESSI, C.M.; PIOLA, A.P.; HENRICH, R. Holocene changes in Antarctic Intermediate Water flow strength in the Southwest Atlantic. **Palaeogeography, Palaeoclimatology, Palaeoecology**, v. 463, p. 60-67, 2016. DOI: 10.1016/j.palaeo.2016.09.018.

WAINER, I.; GOES, M.; MURPHY, L. N.; BRADY, E. Changes in the intermediate water mass formation rates in the global ocean for the Last Glacial Maximum, mid-Holocene and pre-industrial climates. **Paleoceanography**, v. 27, n. 3, 2012. DOI:10.1029/2012pa002290.

10 APPENDIX A – TABLES OF DATA FROM CORE M125-78-2

Core	Depth (cm)	Age yrs BP (median)	$\delta^{13}C$ (*C. incrassatus*)	$\delta^{18}O$ (*C. incrassatus*)	$\delta^{13}C$ (*N. dutertrei*)	$\Delta\delta^{13}C_{pl\text{-}epi}$	TOC (%)
M125-78-2	0-0.5	2183.4	1.26	2.04	2.20	0.94	1.46
M125-78-2	0.5-1	2605.9	1.13	2.71	2.03	0.90	1.13
M125-78-2	1-2	3027.3	1.35	2.43	1.67	0.31	1.17
M125-78-2	2-3	3871.3	1.42	2.55	1.98	0.56	0.87
M125-78-2	3-4	4720.3	1.24	2.84	2.17	0.93	0.85
M125-78-2	4-5	5567.8	1.52	2.29	1.52	0.01	0.74
M125-78-2	5-6	6412.3	1.36	2.51	1.71	0.35	0.63
M125-78-2	6-7	6558.9	1.16	2.64	1.77	0.61	0.68
M125-78-2	7-8	6703.1	0.87	3.28	1.91	1.04	0.59
M125-78-2	8-9	6849.4	1.15	3.01	1.41	0.27	0.60
M125-78-2	9-10	6994.9	0.94	3.12	1.78	0.83	0.66
M125-78-2	10-11	7137.1	0.87	2.55	1.85	0.98	---
M125-78-2	11-12	7278.1	0.82	2.81	1.71	0.89	0.77
M125-78-2	12-13	7413.3	0.96	2.85	1.79	0.82	---
M125-78-2	13-14	7540.9	0.87	2.39	2.24	1.37	0.86
M125-78-2	14-15	7664.3	0.99	2.54	1.88	0.89	---

Core	Depth (cm)	Age yrs BP (median)	SAND (%)	SILT (%)	CLAY (%)	SS (µm)	SS%	$CaCO_3$ (%)	Sedimentation Rate (cm/ka)	BFAR (ind.cm^{-2}.ka^{-1})
M125-78-2	0-0.5	2183.4	3.52	70.99	25.49	32.41	51.71	70.21	2.14	76936.6
M125-78-2	0.5-1	2605.9	1.08	59.52	39.4	27.59	36.55	65.34	1.18	50168.0
M125-78-2	1-2	3027.3	2.65	60.36	36.99	30.84	40.48	65.22	2.37	18668.7
M125-78-2	2-3	3871.3	0.73	58.41	40.86	27.56	31.15	64.21	1.18	10812.8
M125-78-2	3-4	4720.3	3.25	60.42	36.33	31.84	40.45	65.03	1.18	20279.2
M125-78-2	4-5	5567.8	2.85	64.49	32.66	31.88	41.90	63.72	1.18	17224.8
M125-78-2	5-6	6412.3	1.1	64.41	34.49	29.06	41.00	69.21	1.18	21584.4
M125-78-2	6-7	6558.9	3.44	65.17	31.39	32.39	42.96	62.90	6.82	93635.7
M125-78-2	7-8	6703.1	2.53	64.9	32.57	31.56	43.82	58.81	6.93	130090.2
M125-78-2	8-9	6849.4	0.67	67.8	31.53	25.62	42.11	59.34	6.84	76213.3
M125-78-2	9-10	6994.9	0.0	57.37	42.63	22.22	28.26	54.97	6.87	94749.1
M125-78-2	10-11	7137.1	0.0	69.67	30.33	15.32	39.29	38.77	7.03	39261.6
M125-78-2	11-12	7278.1	0.0	69.07	30.93	16.91	42.25	24.25	7.09	15553.2
M125-78-2	12-13	7413.3	0.0	70.96	29.04	16.51	43.35	32.15	7.40	46590.2
M125-78-2	13-14	7540.9	0.0	70.61	29.39	18.31	42.14	48.70	7.84	67531.3
M125-78-2	14-15	7664.3	0.0	70.95	29.05	17.16	42.82	45.63	8.10	50081.0

11 APPENDIX B – TABLES OF DATA FROM CORE M125-77-2

Core	Depth (cm)	Age yrs BP (median)	$\delta^{13}C$ (*C. incrassatus*)	$\delta^{18}O$ (*C. incrassatus*)	$\delta^{13}C$ (*N. dutertrei*)	$\Delta\delta^{13}C_{pl\text{-}epi}$	TOC (%)
M125-77-2	0-0.5	1667	1.40	2.70	1.73	0.33	1.86
M125-77-2	0.5-1	1846	1.16	2.14	2.10	0.94	1.56
M125-77-2	1-2	2026	1.49	3.00	2.17	0.68	1.41
M125-77-2	2-3	2383	1.39	2.79	2.13	0.74	1.41
M125-77-2	3-4	2736	1.19	2.65	1.93	0.74	1.42
M125-77-2	4-5	3088	1.25	2.80	1.76	0.51	1.42
M125-77-2	5-6	3438	1.28	2.67	1.95	0.67	1.18
M125-77-2	6-7	4557	1.41	2.86	1.82	0.41	0.89
M125-77-2	7-8	5677	1.32	2.89	1.77	0.45	0.97
M125-77-2	8-9	6790	1.46	2.91	1.88	0.41	0.92
M125-77-2	9-10	7905	1.23	2.99	2.19	0.96	0.87
M125-77-2	10-11	9019	1.36	3.14	2.34	0.98	---
M125-77-2	11-12	9553	1.32	2.92	2.23	0.90	1.43
M125-77-2	12-13	10086	1.21	3.10	1.94	0.73	---
M125-77-2	13-14	10616	1.31	3.21	1.78	0.48	1.02
M125-77-2	14-15	11137	1.37	3.02	2.03	0.65	---
M125-77-2	15-16	11658	1.00	3.02	2.25	1.25	0.68
M125-77-2	16-17	12518	1.20	3.13	2.00	0.80	---
M125-77-2	17-18	13380	1.13	3.06	2.06	0.93	0.68
M125-77-2	18-19	14232	1.21	3.43	2.12	0.91	---
M125-77-2	19-20	15079	1.28	4.26	2.10	0.82	0.57
M125-77-2	20-21	15925	0.98	3.84	1.81	0.83	---
M125-77-2	21-22	17622	1.19	3.83	1.73	0.53	---
M125-77-2	22-23	19318	0.91	3.95	2.02	1.11	0.55
M125-77-2	23-24	21016	1.16	3.50	2.15	0.98	---
M125-77-2	24-25	22711	1.15	3.94	1.99	0.84	0.66

Core	Depth (cm)	Age yrs BP (median)	SAND (%)	SILT (%)	CLAY (%)	SS (µm)	SS%	$CaCO_3$ (%)	Sedimentation Rate (cm/ka)	BFAR (ind.cm^{-2}. ka^{-1})
M125-77-2	0-0.5	1667	0.0	61.71	38.29	15.14	31.55	77.7	1.77	8788.0
M125-77-2	0.5-1	1846	0.0	61.73	38.27	16.30	32.25	80.1	2.79	14058.7
M125-77-2	1-2	2026	0.0	57.11	42.89	15.21	27.59	75.9	5.56	13188.9
M125-77-2	2-3	2383	0.0	57.31	42.69	15.19	28.09	76.7	2.80	6453.8
M125-77-2	3-4	2736	0.0	57.15	42.85	14.49	27.55	78.5	2.83	5297.5
M125-77-2	4-5	3088	0.0	59.66	40.34	14.83	29.95	80.7	2.84	7173.3
M125-77-2	5-6	3438	0.0	61.63	38.37	16.64	33.75	79.3	2.86	12811.4
M125-77-2	6-7	4557	0.0	65.81	34.19	18.46	37.51	71.7	0.89	3528.2
M125-77-2	7-8	5677	0.0	59.76	40.24	17.80	30.75	81.5	0.89	3142.9
M125-77-2	8-9	6790	0.0	57.5	42.5	16.51	29.96	74.4	0.90	3330.6
M125-77-2	9-10	7905	0.0	52.68	47.32	16.32	25.66	71.1	0.90	5063.7
M125-77-2	10-11	9019	0.1	60.69	39.25	25.14	41.02	74.8	0.90	2281.0
M125-77-2	11-12	9553	0.0	67.99	32.01	21.22	42.79	75.2	1.87	6217.2
M125-77-2	12-13	10086	0.0	63.07	36.93	23.11	42.48	45.2	1.88	5303.9
M125-77-2	13-14	10616	0.0	66.56	33.44	20.91	44.81	72.8	1.89	7790.6
M125-77-2	14-15	11137	0.0	59.47	40.53	14.94	24.22	56.2	1.92	5048.0
M125-77-2	15-16	11658	0.0	54.21	45.79	14.01	19.88	52.8	1.92	4646.8
M125-77-2	16-17	12518	0.0	66.29	33.71	15.04	32.72	53.3	1.16	3455.8
M125-77-2	17-18	13380	0.0	40.95	59.05	14.75	16.09	53.3	1.16	3142.7
M125-77-2	18-19	14232	0.0	73.09	26.91	22.50	52.61	51.4	1.17	2334.5
M125-77-2	19-20	15079	0.0	48.87	51.13	11.90	13.30	47.3	1.18	2955.1
M125-77-2	20-21	15925	0.0	65.38	34.62	14.65	28.61	46.7	1.18	2637.1
M125-77-2	21-22	17622	0.0	68.49	31.51	14.33	33.96	40.3	0.59	940.5
M125-77-2	22-23	19318	0.0	50.85	49.15	17.02	23.90	45.0	0.59	778.3
M125-77-2	23-24	21016	0.0	77.33	22.64	25.58	62.62	45.2	0.59	1017.7
M125-77-2	24-25	22711	0.0	55.38	44.62	22.98	31.05	44.4	0.59	1011.2

12 APPENDIX C – SEDIMENTOLOGICAL DATA GRAPHS

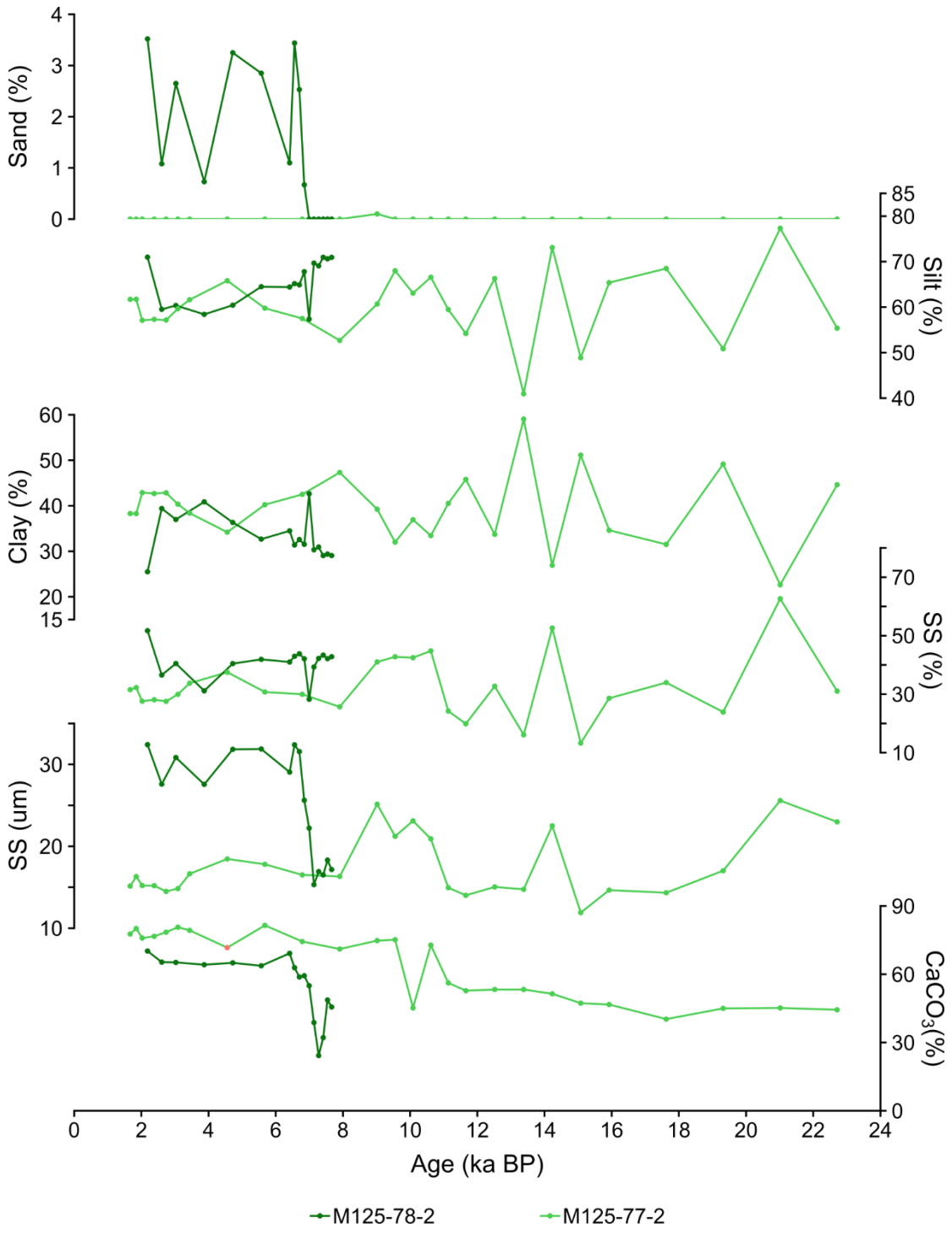

13 APPENDIX D – ROSE BENGAL DILUTED SAMPLES VOLUME CORRECTION TABLES

Core	Depth (cm)	D_r	%SED	%HUM	V_d	W_d	W_t	D_d	V_{rs}	W_{rs}	W_r	V_r
M125-78-2	0-0.5	0.95	54.36	45.64	2.00	0.54	1.00	0.50	20.00	10.00	5.44	5.70
M125-78-2	0.5-1	0.71	53.07	46.93	2.00	0.33	0.62	0.31	19.00	5.91	3.14	4.39
M125-78-2	1-2	0.85	55.69	44.31	2.60	1.07	1.92	0.74	10.50	7.76	4.32	5.06
M125-78-2	2-3	0.93	55.50	44.50	2.50	1.31	2.36	0.95	11.00	10.40	5.77	6.23
M125-78-2	3-4	0.94	57.85	42.15	2.60	1.67	2.89	1.11	10.50	11.68	6.76	7.22
M125-78-2	4-5	0.84	59.93	40.07	2.50	1.41	2.36	0.94	10.00	9.43	5.65	6.76
M125-78-2	5-6	1.01	60.57	39.43	2.50	1.45	2.40	0.96	10.50	10.09	6.11	6.08
M125-78-2	6-7	0.88	57.05	42.95	2.40	1.43	2.51	1.05	10.00	10.46	5.97	6.80
M125-78-2	7-8	0.95	60.29	39.71	2.20	0.98	1.62	0.74	10.50	7.74	4.67	4.90
M125-78-2	8-9	1.00	58.85	41.15	2.20	0.88	1.50	0.68	10.50	7.16	4.21	4.20
M125-78-2	9-10	0.99	61.24	38.76	2.30	0.81	1.32	0.57	10.00	5.74	3.51	3.55

Core	Depth (cm)	D_r	%SED	%HUM	V_d	W_d	W_t	D_d	V_{rs}	W_{rs}	W_r	V_r
M125-77-2	0-0.5	0.40	42.79	57.21	1.4	0.21	0.49	0.35	20.0	7.02	3.00	2.34
M125-77-2	0.5-1	0.72	49.43	50.57	1.4	0.19	0.38	0.27	20.0	5.38	2.66	2.02
M125-77-2	1-2	0.79	53.13	46.87	2.4	0.89	1.67	0.70	10.0	6.98	3.71	1.88
M125-77-2	2-3	0.60	44.70	55.30	2.2	0.78	1.74	0.79	11.0	8.70	3.89	2.24
M125-77-2	3-4	0.54	43.88	56.12	2.0	0.80	1.82	0.91	10.5	9.53	4.18	2.28
M125-77-2	4-5	0.57	41.20	58.80	2.5	0.95	2.32	0.93	11.0	10.20	4.20	2.43
M125-77-2	5-6	0.58	44.08	55.92	2.2	0.81	1.83	0.83	10.5	8.75	3.86	2.27
M125-77-2	6-7	0.72	50.76	49.24	2.4	1.11	2.19	0.91	11.0	10.04	5.10	1.97
M125-77-2	7-8	0.78	52.69	47.31	2.5	1.00	1.90	0.76	10.0	7.62	4.01	1.90
M125-77-2	8-9	0.74	50.71	49.29	2.4	0.94	1.85	0.77	11.0	8.46	4.29	1.97
M125-77-2	9-10	0.86	54.73	45.27	2.1	0.72	1.31	0.62	10.5	6.55	3.58	1.83
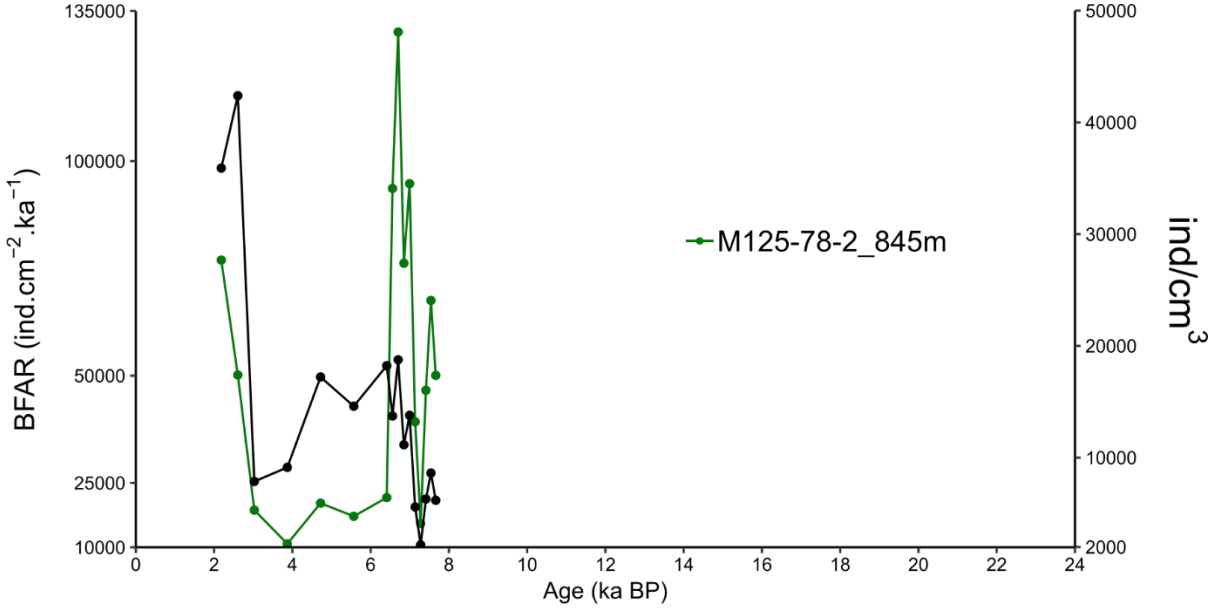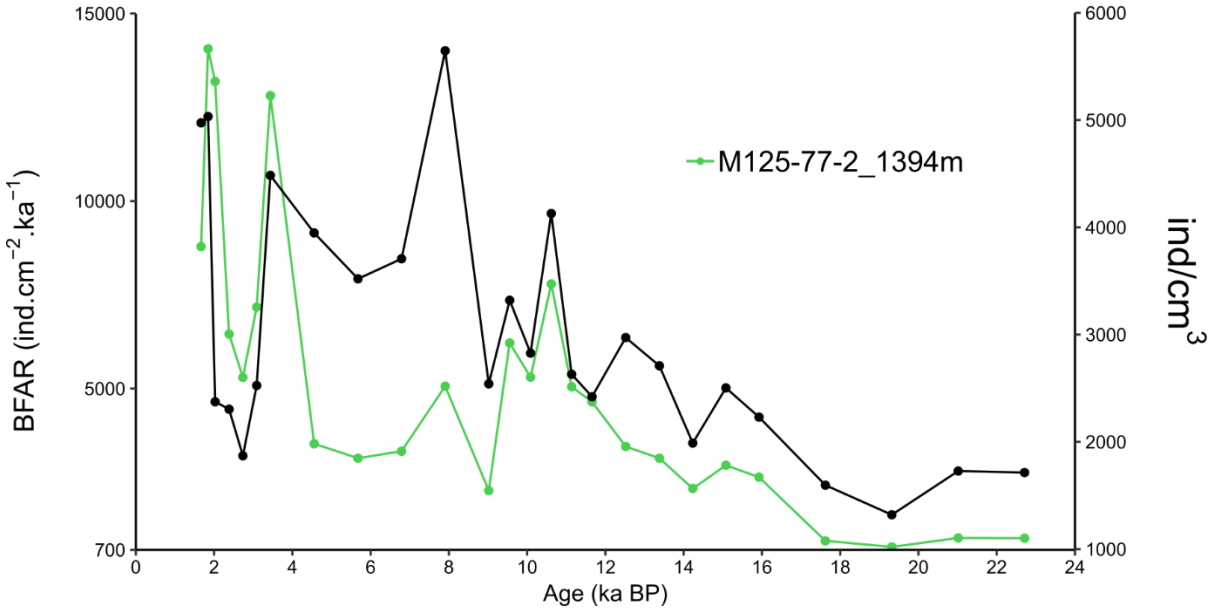
14 APPENDIX E – BFAR GRAPH WITH ESTIMATED BENTHIC FORAMINIFERA INDIVIDUALS PER CM³